

Ocean acoustic tomography based on peak arrivals

E. K. Skarsoulis

*Institute for Applied and Computational Mathematics, Foundation for Research and Technology Hellas,
P.O. Box 1527, 711 10 Heraklion, Crete, Greece*

G. A. Athanassoulis

*Department of Naval Architecture and Marine Engineering, National Technical University of Athens,
P.O. Box 64070, 157 10 Zografos, Greece and Institute for Applied and Computational Mathematics,
Foundation for Research and Technology Hellas, P.O. Box 1527, 711 10 Heraklion, Crete, Greece*

U. Send

Institut für Meereskunde, Universität Kiel, Düsterbrook Weg 20, 24105 Kiel, Germany

(Received 28 June 1995; accepted for publication 3 December 1995)

The recently introduced notion of peak arrivals [Athanassoulis and Skarsoulis, *J. Acoust. Soc. Am.* **97**, 3575–3588 (1995)], defined as the significant local maxima of the arrival pattern, is studied here as a modeling basis for performing ocean tomography. Peak arrivals constitute direct theoretical counterparts of experimentally observed peaks, and offer a complete modeling of experimental observables, even in cases where ray or modal arrivals cannot be resolved. The coefficients of the resulting peak-inversion system, relating travel-time with sound-speed perturbations, are explicitly calculated in the case of range-independent environments using normal-mode theory. To apply the peak-inversion scheme to tomography the peak identification and tracking problem is examined from a statistical viewpoint; maximum-likelihood and least-square solutions are derived and discussed. The particular approach adopted treats the identification and tracking problem in close relation to the inversion procedure; all possibilities of associating observed peaks with background arrivals are examined via trial inversions, and the best peak identification is selected with respect to a least-square criterion. The feasibility of peak tomography is subsequently demonstrated using first synthetic data and then measured data from the THETIS-I experiment. In the synthetic case the performance of the overall scheme is found to be satisfactory both with noise-free and noisy data. Furthermore, the identification, tracking, and inversion results using experimental acoustic data from THETIS-I are in good agreement with independent field observations. © 1996 Acoustical Society of America.

PACS numbers: 43.30.Pc, 43.30.Bp, 43.60.Cg, 43.60.Rw [JHM]

INTRODUCTION

Ocean acoustic tomography based on travel-time perturbations was introduced by Munk and Wunsch¹ in 1979 as a tool for monitoring the sea environment. It has been traditionally implemented by using ray-theoretic modeling, in which arrival times are modeled as travel times along eigen-rays connecting source and receiver (ray arrivals).^{2–6} Their variations are associated with variations of the sound speed along ray paths, forming the basis of the corresponding ray-inversion scheme (ray tomography). Ray theory is simple to apply and also offers a lot of insight into the structure of the received signals and the geometry of the insonified water areas. Yet, ray tomography occasionally suffers from limitations, either due to lack of ray resolvability (usually among late arrivals),^{6,7} or due to the insufficiency of the ray approximation, e.g., in the low-frequency case.⁸

An alternative approach, also proposed by Munk and Wunsch,¹ is modal tomography.^{6,9–11} In this context, observed peaks in the received signal are associated with arrivals of specific propagating modes (modal arrivals). Further, using group-velocity considerations, the corresponding travel-time perturbations are associated with the underlying sound-speed perturbations, giving rise to a modal-inversion

scheme. Mode theory gives an exact representation of the acoustic field, and in this sense it offers a remedy to possible deficiencies of the ray approximation. Nevertheless, the identification of modal arrivals in realistic arrival patterns, generated by finite-bandwidth transmissions in deep-water environments, is not in general possible, even for late arrivals, corresponding to a small number of low-order modes.^{7,12}

Recently a new approach for modeling arrival-time perturbations has been contrived and implemented by the first two authors,¹³ which is called the *peak-arrival* approach. In this approach, arrival times are defined as the time instants τ_i , $i=1, \dots, I$, corresponding to the significant peaks (maxima) of the arrival pattern. Using this definition, the calculation of arrival-time perturbations with respect to a reference (background) situation can be analytically performed by calculating the appropriate Fréchet derivatives of the point functionals τ_i with respect to the sound-speed field. The peak-arrival approach is in full correspondence with experimental practice, peak arrivals being the exact theoretical counterparts of the experimental observables. Furthermore, it does not require the interpretation of actual (observed) peaks as ray or modal arrivals. On this basis, a perturbative inversion scheme can be formulated that is free from any restrictions posed by the conditions of mode or ray resolvability.

On the other hand, comparative studies of peak arrivals with ray arrivals¹³ and modal arrivals¹⁴ illustrated that the notion of peak arrivals encompasses the other two, in the sense that peak arrivals coincide with ray or modal ones in case of ray or mode resolvability, respectively.

To use peak arrivals in tomography, also the peak identification problem, i.e., association of observed peaks with background peak arrivals, has to be addressed.^{15,16} Traditionally this problem is solved by first obtaining peak tracks (tracking problem), i.e., following the observed peaks from one reception to another by some pattern recognition method, and then associating the tracked peaks with some of the background arrivals (identification problem). Although this approach is successful in cases of stable and well-separated peaks,¹⁷ tracking becomes ambiguous in the case of peaks fading in/out or close to the resolution limit. Various tracking methods have been developed to treat such ambiguous cases, based, e.g., on additional arrival-angle information,^{4,18} adaptive filtering,^{19,20} or statistical decision theory.^{21,22} A unified approach is adopted here for the peak identification and tracking problem, which was first developed in the context of ray tomography by the third author.²³ In this approach the peak identification problem is treated in close relation to the inversion problem; all possibilities of associating observed peaks with background arrivals are tested via trial inversions, and finally the best identification is selected with respect to a least-square criterion. The method is extended here to treat peak arrivals and it is also examined from the statistical point of view (peak identification as a problem of statistical estimation), to allow for a more complete interpretation.

The contents of the present work are organized as follows: In Sec. I the notion of peak arrivals is mathematically formulated and perturbation formulas relating peak-arrival displacements with sound-speed perturbations are given. In Sec. II the inversion problem is addressed, and the method of stochastic inversion based on maximum-likelihood estimation is briefly reviewed. A first application of the peak-inversion scheme using synthetic data is also presented in this section. The synthetic test case is motivated from the THETIS-I tomographic experiment conducted in Winter 1991–1992 in the western Mediterranean Sea.²⁴ In Sec. III the problem of peak identification and tracking is dealt with, from the statistical and least-square point of view. Results of the proposed identification/tracking scheme are presented for the synthetic test case, using both noise-free and noisy data. In Sec. IV the peak identification, tracking, and inversion scheme is applied to measured data from the THETIS-I tomographic experiment and the results are compared with independent field observations. Finally, Sec. V contains a discussion on the capabilities and limitations of peak tomography as well as the main conclusions from this work.

I. PEAK ARRIVALS

A. Arrival pattern and peak arrivals

In the framework of linear acoustics, the ocean sound channel intervening between a source (s) and a receiver (r) can be considered as a linear system with transfer function

$H_{sr}(\omega) = G(\mathbf{r}_r; \mathbf{r}_s; \omega)$, the Green's function of the studied environment; \mathbf{r}_s and \mathbf{r}_r denote the source and receiver location, respectively, and ω denotes the circular frequency. If the source excitation function in the frequency domain is $P_s(\omega)$, the signal at the receiver is a complex function $P_r(\omega)$ given by

$$P_r(\omega) = H_{sr}(\omega) P_s(\omega). \quad (1)$$

The received signal in the time domain can be obtained by taking the inverse Fourier transform of (1),

$$p_r(t) = \frac{1}{2\pi} \int_{-\infty}^{+\infty} H_{sr}(\omega) P_s(\omega) e^{j\omega t} d\omega. \quad (2)$$

The amplitude $a(t) = |p_r(t)|$ is called the *arrival pattern*; if the emitted signal in the time domain is a pulsed signal, then $a(t)$ consists, in general, of a sequence of peaks, called *arrivals*, whose shape and temporal locations (arrival times) τ_i , $i = 1, 2, \dots, I$, are dependent mainly on the sound-speed distribution within the water column. The arrival times τ_i , being the most stable and reliable characteristics of the arrival pattern, constitute a basic set of observables in tomographic experiments. Their perturbations $\delta\tau_i$, $i = 1, 2, \dots, I$, are used in travel-time tomography for the retrieval of the underlying sound-speed perturbations, with respect to a particular background condition.

This is a simplified, yet sufficient, description of the ocean-tomography modeling problem, neglecting signal processing issues of importance for the experimental implementation,^{1,6,25} but not essential for modeling purposes (e.g., in practice the received signals are not considered on their own but they are match-filtered, i.e., cross-correlated with a replica of the emitted signal;^{12,26,27} equivalent expressions as above hold for the corresponding correlated quantities in the time-lag domain¹³).

Peak arrivals are defined as the significant local maxima of the arrival pattern, and peak-arrival times are the time instants τ_i , $i = 1, 2, \dots, I$, corresponding to these maxima.¹³ The key point, to be stressed here, is that the analytical definition of peak arrivals and the corresponding arrival times exactly “imitates” the procedure followed in experimental practice for obtaining arrivals and arrival times. As a consequence, peak arrivals need not be *a priori* associated with specific rays or modes, as is usually tried in traditional tomography. Thus their applicability is not subject to any ray/mode-resolvability limitations. Moreover, the peak-arrival approach is free of any restrictive conditions or hypotheses concerning the signal, the environment, or the wave-propagation model. Of course, the usefulness of peak arrivals and peak-arrival times in ocean tomography is dependent on the ability to analytically calculate perturbations of the latter with respect to sound-speed variations. This issue has been thoroughly studied in a previous work,¹³ where an efficient perturbation formula has been obtained and tested against direct numerical calculations. The basic results of that analysis are summarized in the following two subsections.

B. Arrival-time perturbations: The direct problem

Assume that the actual sound-speed field $c(\mathbf{r})$ can be represented by means of a modal expansion of the form

$$c(\mathbf{r}) = c_0(\mathbf{r}) + \sum_l \vartheta_l \phi_l(\mathbf{r}), \quad (3)$$

where $c_0(\mathbf{r})$ represents a reference sound-speed field, $\phi_l(\mathbf{r})$ constitute a set of sound-speed modes, and ϑ_l are the corresponding modal parameters. The sound-speed modes may consist of empirical orthogonal functions (EOFs), oceanographic modes, or even simple elements of a basis (e.g., triangular or box functions) spanning the space in which the solution is expected to belong. In order to indicate the parametric dependence of the sound-speed field on $\boldsymbol{\vartheta} = \{\vartheta_l\}$, the vector of modal parameters, we shall write $c(\mathbf{r}; \boldsymbol{\vartheta})$. Let $c_b(\mathbf{r}) = c(\mathbf{r}; \boldsymbol{\vartheta}_b)$ be the background sound-speed field, around which we consider perturbations. Accordingly, the actual sound-speed field, considered as a perturbation of the background field, can be written in the form

$$c(\mathbf{r}; \boldsymbol{\vartheta}) = c_b(\mathbf{r}) + \sum_l \delta \vartheta_l \phi_l(\mathbf{r}) = c(\mathbf{r}; \boldsymbol{\vartheta}_b + \delta \boldsymbol{\vartheta}), \quad (4)$$

where $\delta \boldsymbol{\vartheta} = \boldsymbol{\vartheta} - \boldsymbol{\vartheta}_b$ is the perturbation of the parameter vector with respect to the background condition. The arrival times τ_i , corresponding to the background conditions ($\boldsymbol{\vartheta} = \boldsymbol{\vartheta}_b$), satisfy the equation

$$\dot{a}(\tau_i; \boldsymbol{\vartheta}_b) = 0, \quad (5)$$

where a dot denotes differentiation with respect to time t . Equation (5) is a necessary condition for a local maximum of $a(t)$. The restriction to the more significant peaks is carried out by direct inspection of the arrival pattern. The perturbed arrival times $\tau_i + \delta \tau_i$, corresponding to the actual sound-speed field, considered as a perturbation of the background profile ($\boldsymbol{\vartheta} = \boldsymbol{\vartheta}_b + \delta \boldsymbol{\vartheta}$), will then satisfy the equation

$$\dot{a}(\tau_i + \delta \tau_i; \boldsymbol{\vartheta}_b + \delta \boldsymbol{\vartheta}) = 0. \quad (6)$$

A first-order Taylor expansion of this equation, in connection with Eq. (5), finally gives the equation

$$\delta \tau_i = - \sum_l \frac{\partial \dot{a}(\tau_i; \boldsymbol{\vartheta}_b) / \partial \vartheta_l}{\ddot{a}(\tau_i; \boldsymbol{\vartheta}_b)} \delta \vartheta_l = \sum_l B_{il} \delta \vartheta_l. \quad (7)$$

This equation relates sound-speed perturbations ($\delta \vartheta_l$) with induced arrival-time perturbations ($\delta \tau_i$), to the first order. The kernel matrix $\{B_{il}\}$, called the influence matrix,^{13,28} quantifies the influence of the sound-speed modes $\{\phi_l\}$ on the arrival times $\{\tau_i\}$. For its evaluation the second-order time derivative $\ddot{a}(\tau_i; \boldsymbol{\vartheta}_b)$ of the arrival pattern and also the mixed derivative $\partial \dot{a}(\tau_i; \boldsymbol{\vartheta}_b) / \partial \vartheta_l$ have to be calculated.

The background arrival pattern $a(t)$ and the corresponding peak-arrival times τ_i , $i = 1, \dots, I$, can be obtained from (2) if the transfer function $H_{sr}(\omega; \boldsymbol{\vartheta}_b)$ is known, within the signal bandwidth. Further, the time derivatives of $a(t)$ appearing in (7) can be also obtained from $H_{sr}(\omega; \boldsymbol{\vartheta}_b)$ by using elementary properties of the Fourier transform.¹³ Finally, the calculation of the mixed derivative $\partial \dot{a}(\tau_i; \boldsymbol{\vartheta}_b) / \partial \vartheta_l$ can be reduced to the calculation of $H_{sr}(\omega; \boldsymbol{\vartheta}_b)$ and $\partial H_{sr}(\omega; \boldsymbol{\vartheta}_b) / \partial \vartheta_l$. Thus, for the calculation of the influence

coefficients B_{il} , the knowledge of the background transfer function H_{sr} and its derivatives $\partial H_{sr} / \partial \vartheta_l$, in the directions of the sound-speed modes ϕ_l , is required.

The perturbation formula (7) is an essential result for the peak-arrival approach, relating sound-speed perturbations with induced arrival-time perturbations, arrival times being defined as stationary points corresponding to significant maxima of the arrival pattern. From its derivation it is clear that (7) is not subject to any restrictive assumptions concerning the acoustic signal, the environment through which the sound propagates, or the propagation model that is to be used.

C. Implementation for range-independent environments

Analytic expressions for H_{sr} and $\partial H_{sr} / \partial \vartheta_l$ can be obtained for the case of range-independent environments ($c = c(z; \boldsymbol{\vartheta})$, $\phi_l = \phi_l(z)$), by using normal-mode theory.¹³ For completeness, the final results of the corresponding analysis are given below.

Let a harmonic point source of unit strength and circular frequency ω be located on the z axis at a depth $z = z_s$ from the sea surface, and a receiver be located at a range R from the source and at a depth $z = z_r$ (the z axis is considered positive downward). Then, if the range R is sufficiently long, the acoustic complex pressure at the receiver's location, i.e., the acoustic-channel transfer function, can be written in terms of normal modes as^{8,29,30}

$$H_{sr}(\omega; \boldsymbol{\vartheta}_b) = \frac{\omega \rho^2}{\sqrt{8\pi}} \sum_{n=1}^M \frac{u_n(z_s) u_n(z_r)}{\sqrt{k_n R}} \exp\{j k_n R - j \pi/4\}, \quad (8)$$

where ρ is the water density, while k_n and u_n , $n = 1, \dots, M$, are the real eigenvalues and the corresponding eigenfunctions (propagating modes) of the associated vertical Sturm–Liouville problem. In the above expression for H_{sr} , and throughout this subsection, it is understood that $k_n = k_n(\omega; \boldsymbol{\vartheta}_b)$, and $u_n(z) = u_n(z; \omega; \boldsymbol{\vartheta}_b)$, i.e., the eigenvalues and eigenfunctions (modes) are considered for the circular frequency ω and the background environment $\boldsymbol{\vartheta} = \boldsymbol{\vartheta}_b$; writing the full dependences is omitted for conciseness.

The Fréchet derivative of the transfer function H_{sr} with respect to the l th sound-speed mode is given by

$$\frac{\partial H_{sr}(\omega; \boldsymbol{\vartheta}_b)}{\partial \vartheta_l} = - \frac{\omega \rho^2}{\sqrt{8\pi}} \sum_{n=1}^M \left\{ \sum_{m \neq n}^M \frac{Q_{nm}^l U_{nm}}{k_n^2 - k_m^2} + \frac{Q_{nn}^l U_{nn}}{2k_n^2} - \frac{Q_{nn}^l U_{nn}}{k_n} j R \right\} \frac{e^{j k_n R - j \pi/4}}{\sqrt{k_n R}}, \quad (9)$$

where

$$Q_{nm}^l = \int_0^h \rho \omega^2 \frac{\phi_l(z)}{c_b^3(z)} u_n(z) u_m(z) dz, \quad (10)$$

h is the depth of the water column, and

$$U_{nm} = U_{nm}(\omega; \mathbf{\vartheta}_b) = \begin{cases} u_n(z_s)u_m(z_r) + u_n(z_r)u_m(z_s), & \text{for } n \neq m, \\ -\frac{1}{2}u_n(z_r)u_n(z_s), & \text{for } n = m. \end{cases} \quad (11)$$

Thus, for range-independent environments, using expressions (8) and (9), the arrival pattern $a(t)$ and the influence matrix $\{B_{il}\}$ can be calculated analytically.

II. PEAK INVERSION

The first-order perturbation formula (7), relating sound-speed and arrival-time perturbations, can be written in the form

$$\delta\tau_i^{(1)} = \sum B_{il} \delta\vartheta_l, \quad i = 1, 2, \dots, I, \quad (12)$$

where the superscript of $\delta\tau_i$ denotes the validity of the prediction up to the first order. Actual arrival-time perturbations $\delta\tau_i$, on the other hand, differ in general from the above predicted ones (12) by an amount e_i , $i = 1, 2, \dots, I$, associated with modeling and observation errors. Thus we have in general

$$\delta\tau_i = \sum B_{il} \delta\vartheta_l + e_i, \quad i = 1, 2, \dots, I. \quad (13)$$

The aim of ocean acoustic tomography is to infer the sound-speed variations $\{\delta\vartheta_l\}$ by measuring arrival displacements $\{\delta\tau_i\}$. In the light of Eq. (13) this is an inverse problem, in which from given $\{\delta\tau_i\}$ one wishes to estimate the unknown vector $\{\delta\vartheta_l\}$ and also the error vector $\{e_i\}$, which is unknown as well.

In geophysical inverse problems some kind of *a priori* knowledge about the sought quantities is usually available, either in terms of appropriate parametric representation formulas of the solution, depending on a small number of parameters, or in terms of statistical information about these quantities. This *a priori* information can be used as physical constraints, drastically restricting the solution space to a subspace of physically meaningful solutions.

The expansion (4) of the sound-speed field in terms of sound-speed modes (e.g., EOFs or oceanographic modes) was in fact a step in this direction (reduction from an infinite-dimensional function space to a finite-dimensional parameter space). Further reduction of the solution uncertainty can be obtained by exploiting *a priori* statistical information about the corresponding modal amplitudes $\{\delta\vartheta_l\}$ and the error vector $\{e_i\}$. For this purpose, a proper statistical setting is necessary, described in the following.

A. Maximum-likelihood estimation

Let a linear observation system be modeled through the relation

$$\mathbf{y} = \mathbf{B}\mathbf{x} + \mathbf{n}. \quad (14)$$

Equation (14) relates the model vector \mathbf{x} ($\delta\mathbf{\vartheta}$ in our case) with the data vector \mathbf{y} (vector of observables, $\delta\tau_i$) via the matrix \mathbf{B} (the influence matrix) acting from the model space

into the data space. Modeling and observation errors are represented by the noise vector \mathbf{n} . To allow for a statistical description, \mathbf{x} , \mathbf{y} , and \mathbf{n} are considered in the following as zero-mean random vectors; furthermore, \mathbf{x} and \mathbf{n} are assumed statistically independent. The *a priori* information for the model and noise vector consists of the knowledge of the probability density functions $f_X(\mathbf{x})$ and $f_N(\mathbf{n})$ prior to the particular observation; if \mathbf{x} and \mathbf{n} are Gaussian, this information reduces to the knowledge of the corresponding covariance matrices \mathbf{R}_{xx} and \mathbf{R}_{nn} .

By combining the prior information, f_X and f_N , with the model relation (14) the conditional probability density function $f_{X|Y}(\mathbf{x})$ of the model vector \mathbf{x} , given the data vector \mathbf{y} , can be derived. This is called a *a posteriori* probability density function in the model space and it is the heart of the Bayesian approach to inverse problems;^{31,32} its maximization with respect to \mathbf{x} results in the maximum-likelihood or MAP (maximum *a posteriori* probability) estimate of the model vector. Under the Gaussian hypothesis $f_{X|Y}$ takes the form³¹

$$f_{X|Y}(\mathbf{x}) = C_1 \exp\{-\frac{1}{2}S(\mathbf{x})\}, \quad (15)$$

where C_1 is a constant, independent of \mathbf{x} , and $S(\mathbf{x})$ is the quadratic function

$$S(\mathbf{x}) = (\mathbf{B}\mathbf{x} - \mathbf{y})' \mathbf{R}_{nn}^{-1} (\mathbf{B}\mathbf{x} - \mathbf{y}) + \mathbf{x}' \mathbf{R}_{xx}^{-1} \mathbf{x}, \quad (16)$$

where a prime denotes the transpose of a matrix. By defining

$$\hat{\mathbf{x}} = \mathbf{R}_{xx} \mathbf{B}' (\mathbf{B} \mathbf{R}_{xx} \mathbf{B}' + \mathbf{R}_{nn})^{-1} \mathbf{y}, \quad (17)$$

$f_{X|Y}(\mathbf{x})$ can be written in the alternative form

$$f_{X|Y}(\mathbf{x}) = C_2 \exp\{-\frac{1}{2}(\mathbf{x} - \hat{\mathbf{x}})' (\mathbf{B}' \mathbf{R}_{nn}^{-1} \mathbf{B} + \mathbf{R}_{xx}^{-1}) (\mathbf{x} - \hat{\mathbf{x}})\}, \quad (18)$$

where C_2 is a constant, independent of \mathbf{x} . Thus the *a posteriori* probability density function in the model space is Gaussian, with mean value $\hat{\mathbf{x}}$ given by (17) and covariance matrix $\mathbf{D}_{xx} = (\mathbf{B}' \mathbf{R}_{nn}^{-1} \mathbf{B} + \mathbf{R}_{xx}^{-1})^{-1}$. In this case, the maximum-likelihood estimate of the model vector \mathbf{x} is equal to the mean value $\hat{\mathbf{x}}$ of the Gaussian distribution (18),

$$f_{X|Y}(\hat{\mathbf{x}}) = \max_{\mathbf{x}} f_{X|Y}(\mathbf{x}), \quad (19)$$

and it is given by (17). Using the *a posteriori* covariance matrix \mathbf{D}_{xx} rms error estimates can be obtained for the solution uncertainty. Since the estimate $\hat{\mathbf{x}}$ maximizes the function (15), it has to minimize the quadratic function $S(\mathbf{x})$. In the case of diagonal covariance matrices, $S(\mathbf{x})$ becomes

$$S(\mathbf{x}) = \sum_i \frac{[\{\mathbf{B}\mathbf{x}\}_i - y_i]^2}{\text{diag}[\mathbf{R}_{nn}]_i} + \sum_l \frac{x_l^2}{\text{diag}[\mathbf{R}_{xx}]_l}. \quad (20)$$

The quadratic function (20) is of least-square type. It controls the data misfit (first sum) and the size of the model vector components (second sum); the *a priori* information enters (20) through properly normalizing the individual summands by the corresponding variances. A further useful property of the estimator (17), noted here for completeness, is that it constitutes a minimum-variance estimator, among all estimators which are linear functions of \mathbf{y} ,^{33,34} in this connection the estimate $\hat{\mathbf{x}}$ is also known as a Gauss–Markov estimate or stochastic inverse.^{6,35} In conclusion, it is summa-

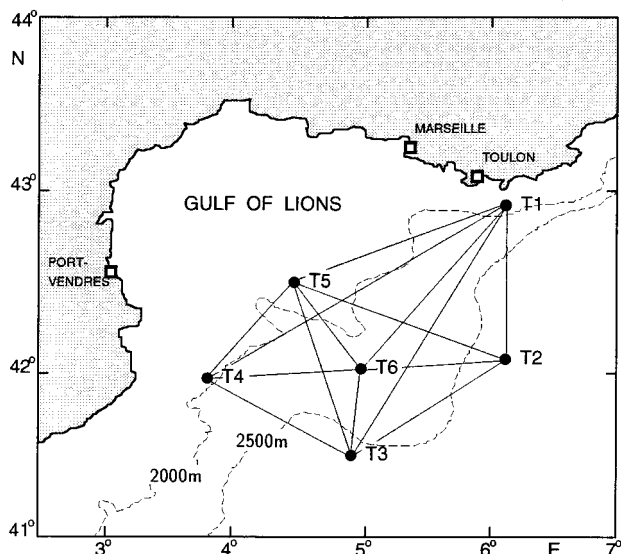


FIG. 1. Location of the THETIS-I experiment and geometry of the tomographic array.

alized that (17) gives the maximum-likelihood (or MAP), minimum-variance, and least-square solution for the case of a linear inverse problem under the Gaussian hypothesis. This estimator will be used in the following for solving the peak-inversion system.

B. A synthetic test case

Before proceeding to tomographic inversions from measured data, a synthetic test case is examined first, in order to assess the performance of the peak-inversion scheme. The synthetic case is motivated from the THETIS-I tomographic experiment²⁴ conducted during winter 1991–1992 in the Gulf of Lions (western Mediterranean Sea); see Fig. 1. An application of the peak-arrival approach to measured data from THETIS-I experiment is presented in Sec. IV.

In particular, the T3–T6 transceiver pair is considered here for reasons discussed in Sec. IV. The model geometry for this pair is shown in Fig. 2. The nominal horizontal distance between T3 and T6 is $R=52\,236$ m. The water depth is taken 2500 m. In order to eliminate bottom effects from the

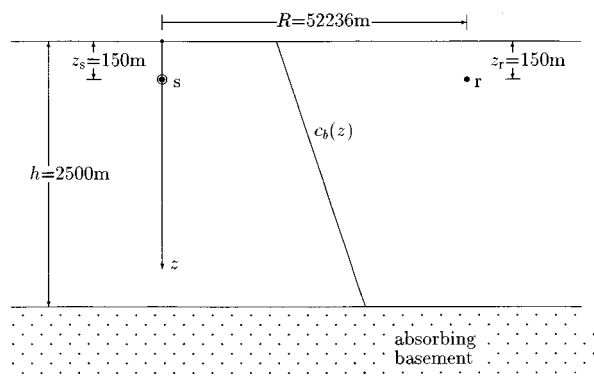


FIG. 2. Model geometry for the T3–T6 transceiver pair.

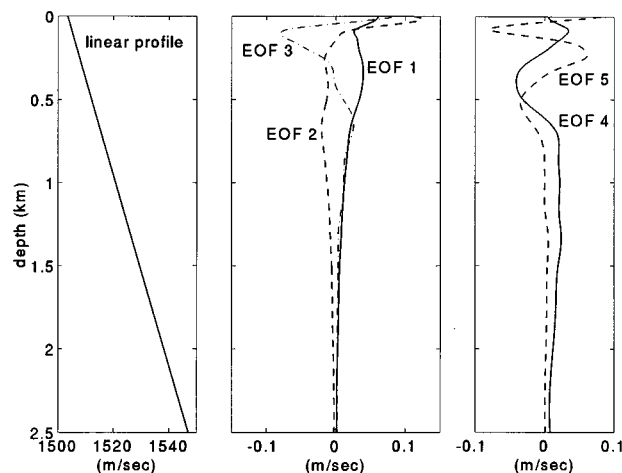


FIG. 3. Linear sound-speed profile and corresponding sound-speed modes (EOFs) obtained from analysis of historical hydrographic data.

received signal an artificial absorbing bottom is considered.¹³ The sound-speed variability in the area of the experiment can be described by a linear reference sound-speed profile, corresponding to homogeneous mixed-layer conditions, and a set of empirical orthogonal functions (EOFs). Figure 3 shows the reference profile and the first five EOFs resulting from principal component analysis of historical hydrographic bottle data for the area. In the subsequent numerical calculations the linear sound-speed profile of Fig. 3 is used as the background profile $c_b(z)$ while the five EOFs are used as sound-speed modes $\phi_l(z)$. Since the background sound-speed profile is taken identical to the reference profile ($c_b=c_0$, $\boldsymbol{\vartheta}_b=0$), the vectors $\boldsymbol{\vartheta}$ and $\delta\boldsymbol{\vartheta}$ coincide below.

For the above environment and geometry the non-bottom-interacting part of the acoustic energy, of interest in ocean tomography, samples the upper 1000 m of the water column; in terms of rays, the steepest RSR (refracted surface-reflected) rays go down to 1000 m.^{13,36} Thus the particular tomographic setting is expected to be insensitive to sound-speed variations below this depth. Furthermore, for the same reason, the exact water depth is not of significance.

For the synthetic calculations a Gaussian impulselike signal of central frequency $f_0=400$ Hz and effective bandwidth $BW=150$ Hz is considered as the emitted signal. The corresponding quantities in the THETIS-I experiment are $f_0=400$ Hz and $BW=100$ Hz; a larger bandwidth is taken in the synthetic case to increase arrival resolution. The arrival pattern corresponding to the linear (background) sound-speed profile is shown in Fig. 4. There are six consecutively numbered peaks in the pattern of Fig. 4, in the time interval between 34.57 and 34.74 s. The final arrival (No. 6) comes from near-axial propagation of acoustic energy and corresponds to low-order modes (shallow rays), while the earlier arrivals (No. 5 to No. 1) are due to propagation of acoustic energy in gradually steeper angles and correspond to higher-order modes (steeper rays). For the implementation of the inverse Fourier transforms (2) via FFT the complex pressure has been calculated in the frequency interval from 300 to 500 Hz with a frequency step of 0.4 Hz to avoid aliasing effects. For the calculation of $H_{sr}(\omega)$ the SuperSNAP normal-mode

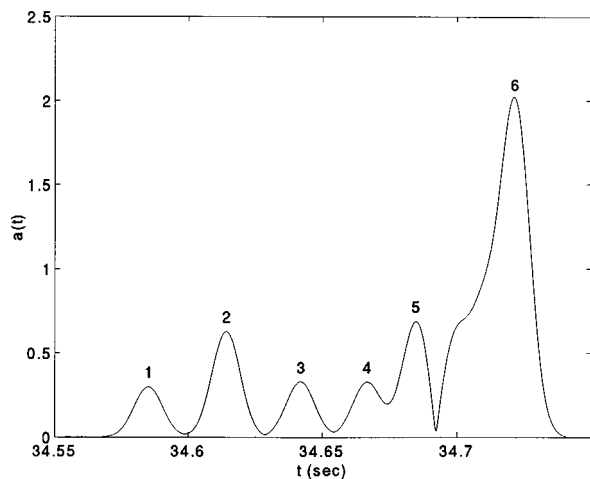


FIG. 4. Background arrival pattern for the linear sound-speed profile.

code has been used.^{37,38} The number of propagating normal modes for the particular environment ranges from 155 (at 300 Hz) to 259 (at 500 Hz).

The Fréchet derivatives $\partial H_{sr}(\omega; \boldsymbol{\vartheta}_b)/\partial \vartheta_l$ have been calculated in a similar manner from Eq. (9), using again Super-SNAP for solving the vertical eigenvalue problem. The resulting influence coefficients B_{il} corresponding to the six peaks of the background arrival pattern and the five EOFs considered ($I=6, L=5$) are shown in Fig. 5. In this figure the horizontal axis serves for identification of the six arrivals (by order and by travel time), whereas the influence coefficients are measured in the vertical axis; points corresponding to the same sound-speed mode are connected by lines for convenience. It is stressed here that the calculation of the influence coefficients is performed in a single direct run [by exploiting the perturbation formula (7) and also expression (9) for the Fréchet derivatives of H_{sr}], rather than using a series of runs for various perturbed sound-speed profiles and forming finite differences over travel times. From Fig. 5 we see that each EOF imposes on the arrival pattern a specific mode of deformation; e.g., EOF 1 causes all arrivals to shift to the same

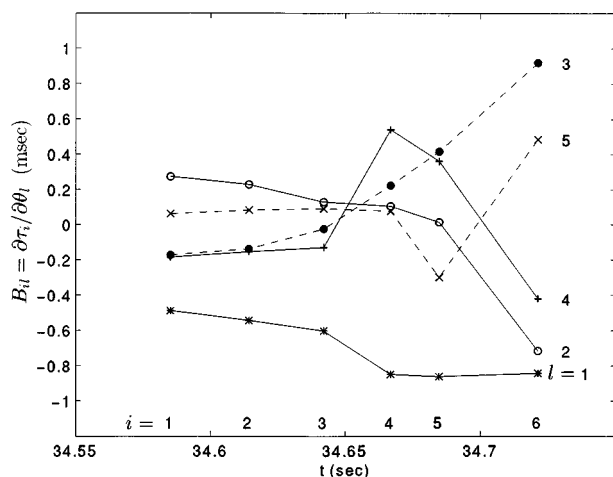


FIG. 5. Influence coefficients corresponding to the five EOFs of Fig. 3 and to the six arrivals of Fig. 4.

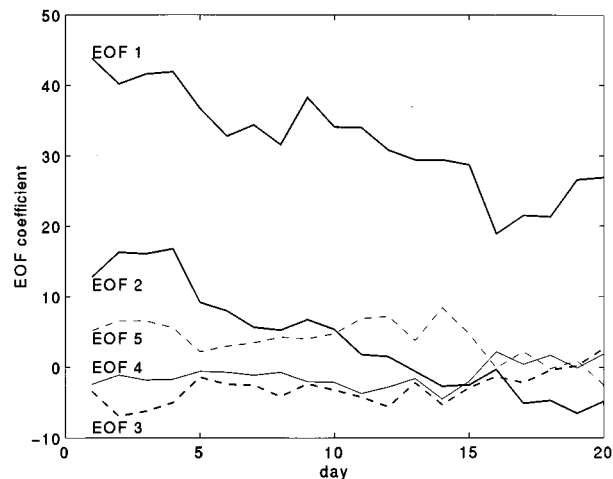


FIG. 6. Time series of the five EOF coefficients, constituting the input data for the synthetic test case.

direction, while EOF 2 causes the first four arrivals to shift in opposite direction from the last arrival and does not affect the time location of peak 5. Below, these EOF fingerprints will help to retrieve the actual EOF coefficients from travel-time data.

In the following, a 20-day episode is synthesized corresponding to typical oceanographic conditions expected during the experiment; see also Sec. IV. The time series of EOF coefficients constituting the synthetic case are shown in Fig. 6. It is seen that the first two EOF coefficients (ϑ_1 and ϑ_2), which are the most significant ones, gradually decrease, thus causing the sound-speed profile to get closer to the linear background profile. The rms values for the five EOF coefficients are $\vartheta_{1,rms}=33$, $\vartheta_{2,rms}=8$, $\vartheta_{3,rms}=4$, $\vartheta_{4,rms}=2$, $\vartheta_{5,rms}=5$. The evolution of sound-speed anomaly profiles (with respect to the linear profile), corresponding to the above EOF coefficients, is shown in Fig. 7. A warm surface layer (ranging down to 100-m depth) and also a subsurface

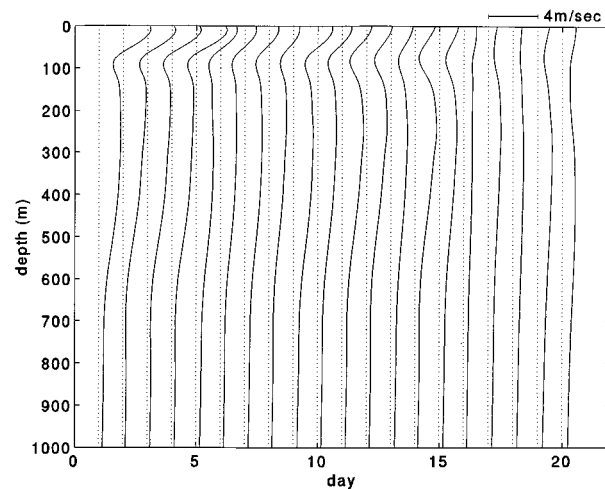


FIG. 7. Evolution of the synthetic sound-speed anomaly profiles, with respect to the linear profile. Reference for each day is marked by dotted lines. The scale for measuring the sound-speed anomalies is given at the top of the figure.

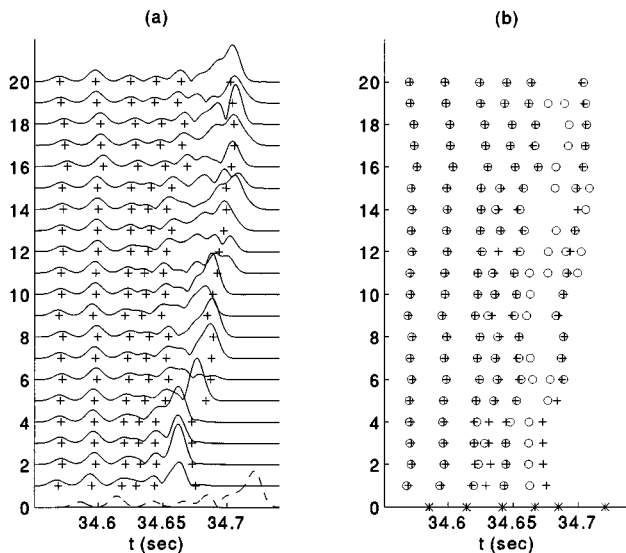


FIG. 8. Comparison of actual peak locations with predicted arrival times, obtained from the first-order perturbation formula and marked by crosses (+), in the 20 receptions of the synthetic case. (a) Evolution of actual arrival patterns; the background arrival pattern is shown at the bottom of the figure (dashed-line pattern). (b) Evolution of actual peak locations, marked by circles (○); the background arrival times are marked by asterisks (*) on the horizontal axis.

layer (between 100 and 600 m) can be seen during the first days of the episode. After day 3 a gradual weakening of these layers, especially of the surface layer, takes place and, finally, the vertical structure is nearly eliminated.

Using the above 20 sound-speed profiles, forward calculations were performed for the arrival pattern. The corresponding 20-day sequence of actual (computed) arrival patterns is shown in Fig. 8(a). At the bottom of this figure the background arrival pattern is also shown (dashed-line pattern). Further, using the perturbation formula (7) along with the EOF coefficients of Fig. 6 and the background arrival times, first-order predictions for actual arrival times were made, corresponding to the six background arrivals; the predicted arrival times are marked by crosses (+) in Fig. 8(a). Figure 8(b) shows the actual arrival times, marked by circles (○), i.e., the time instants corresponding to the maxima of the actual arrival patterns of Fig. 8(a), and again the predicted arrival times are marked by crosses (+). The background arrival times are shown on the horizontal axis of this figure.

From Fig. 8 it is seen that there is a good prediction for the first three arrivals during the whole 20-day period. The prediction for peak 4 is also satisfactory; however, on days 1, 2, 4, and 12 due to closeness between peaks 3 and 4, the latter peak is hidden and the corresponding maximum does not appear at all. Peak 5 is well separated and also quite pronounced, such that it can be clearly seen during the whole period. Its prediction by means of the first-order perturbation formula is satisfactory as well. Finally, the prediction for peak 6 is quite good with an exception of the first four days, in which the actual arrival-time variations are underestimated by nearly 20%, due to the large sound-speed anomalies in the surface layer during the first four days (the final arrival

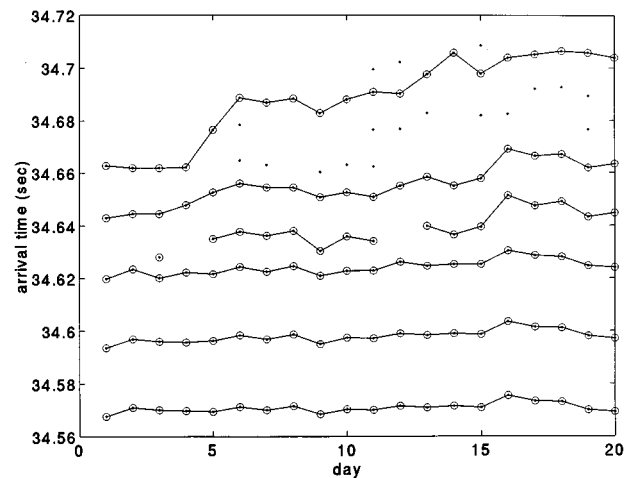


FIG. 9. Manual association of observed peaks, marked by dots (·), and background arrivals. Associated peaks are put in a circle (○). Resulting peak tracks are marked by solid lines.

mainly samples this layer). It is further seen from Fig. 8 that between peaks 5 and 6 there occasionally appear additional peaks in the actual arrival patterns during some days. The present scheme does not treat these peaks since they cannot be assigned to background arrivals. However, they could be treated in the framework of an iterative scheme.

On the basis of the above remarks, and correlating the predicted arrival times with the closest actual ones, six peak tracks can be obtained, as shown in Fig. 9, corresponding to the six background peak arrivals. In Fig. 9 identified peaks are in circles and resulting tracks are marked by solid lines. It is seen that there is no identification for peak 4 on days 1, 2, 4, and 12, and the corresponding track has gaps; cf. previous remarks on Fig. 8. The above way of associating actual peaks with background arrivals exploits the *a priori* knowledge of the underlying sound-speed profiles and corresponding predicted arrival times. This knowledge is available in a synthetic case, but not in a real tomographic experiment where the actual sound speed is the basic unknown. In that case the identification/tracking problem arises, skipped in this section for convenience, and addressed in Sec. III below.

The resulting anomalies between actual and background arrival times are used in the following for the retrieval of the EOF coefficients, by applying the maximum-likelihood inversion scheme described in the previous subsection. The solution-correlation matrix \mathbf{R}_{xx} is taken to be diagonal and its elements are computed from the rms values of the synthetic EOF coefficients. Further, the noise-correlation matrix \mathbf{R}_{nn} is also taken to be diagonal, and the rms values for the prediction errors are taken 1 ms for the first five peaks and 5 ms for the last peak, in accordance with the previous remarks.

In Fig. 10 a comparison of the inversion results for the first three EOF coefficients (dashed lines) with the corresponding input data (solid lines) over the 20-day period is shown. It is seen that the retrieved EOF coefficients are in good agreement with the corresponding synthetic ones. Especially the coefficient of the dominating first EOF is retrieved almost perfectly, throughout the considered period.

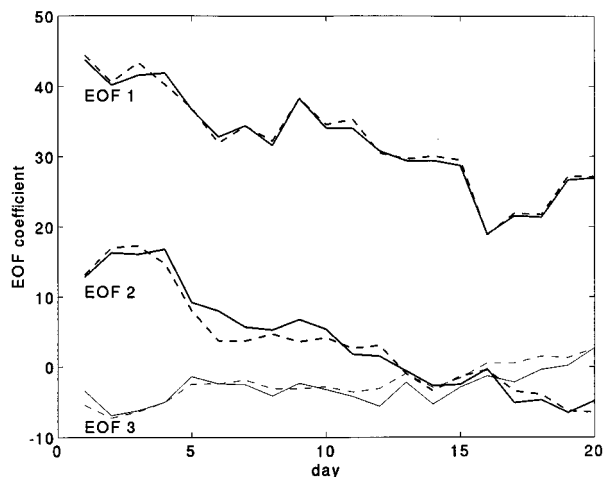


FIG. 10. Comparison of inversion results for the first three EOF coefficients (dashed lines) to the corresponding input data (solid lines), cf. Fig. 6; inversions based on the manually obtained peak tracks of Fig. 9.

The rms values of the solution components are found to be $\hat{\vartheta}_{1,\text{rms}}=33.2$, $\hat{\vartheta}_{2,\text{rms}}=7.9$, $\hat{\vartheta}_{3,\text{rms}}=3.4$, $\hat{\vartheta}_{4,\text{rms}}=1.8$, $\hat{\vartheta}_{5,\text{rms}}=2.3$, compatible with the *a priori* rms values used for the inversion.

A comparison of input and retrieved sound-speed anomaly profiles (with respect to the linear profile) is given in Fig. 11, marked through solid and dashed lines, respectively. From these comparisons it is seen that the peak inversion successfully retrieves the sound-speed evolution within the water column. The largest deviations (about 25% error) occur on days 6 and 9 at the surface. Further comparisons between input data and inversion results are given in Fig. 12, where depth averages of the sound-speed anomalies are shown for three depth layers: 0–100, 100–600, and 0–1000 m. In all three layers the inversion results are in good overall agreement with the synthetic input data; note the satisfactory

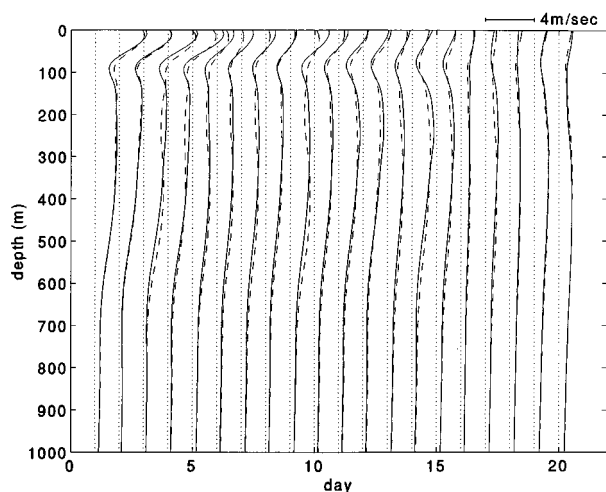


FIG. 11. Comparison between the retrieved sound-speed anomaly profiles, with respect to the linear profile, (dashed lines) and the corresponding synthetic anomaly profiles (solid lines), cf. Fig. 7; inversions based on manually obtained peak tracks.

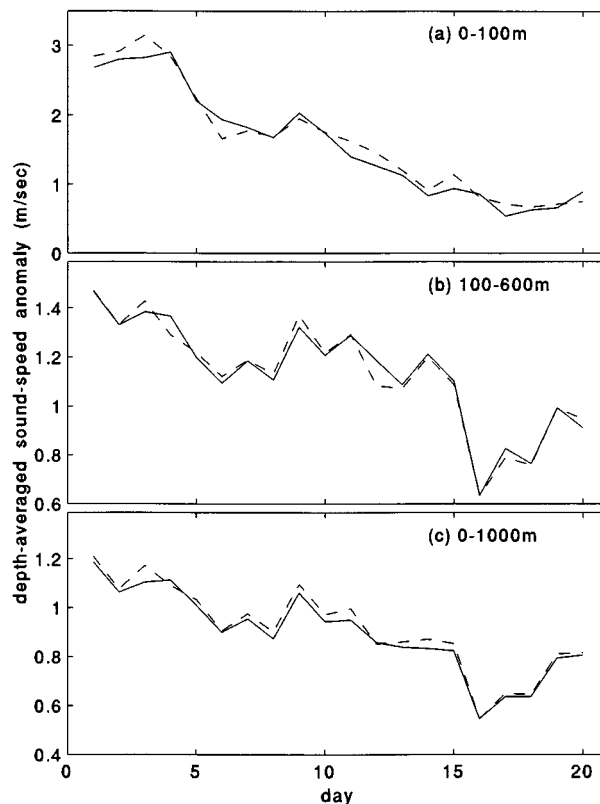


FIG. 12. Comparison of inversion results for the depth-averaged sound-speed anomalies (dashed lines) to the corresponding input anomalies (solid lines); inversions based on manually obtained peak tracks. (a) Layer 0–100 m, (b) layer 100–600 m, (c) Layer 0–1000 m.

agreement in the surface layer during the first days, despite the relatively large prediction errors for peak 6 on these days.

III. PEAK IDENTIFICATION AND TRACKING

In the previous section tracks of identified peaks were obtained by assuming the sound-speed profiles *a priori* known, such that the perturbation formula (7) could be used in a direct way. In a real tomographic experiment, however, the actual sound speed is the basic quantity sought, and hence it cannot be assumed known for identifying peaks and obtaining tracks. Thus the peak-identification problem arises. Its solution traditionally consists of, first, following the observed peaks from one reception to another by using pattern recognition methods (tracking problem); then, the tracked peaks are associated with some of the background arrivals (identification problem); finally, after having identified peak tracks, the inversion problem is addressed.

A unified approach that simultaneously treats the tracking and identification problem, in close relation to the inversion procedure, was recently developed by the third author^{23,36} in the context of ray tomography. The basic idea is to test *all* possibilities of associating observed peaks (above a threshold) in a reception with background arrivals via trial inversions, and finally select the best identification with respect to a least-square criterion. This approach is adopted here, with the modification of using peak arrivals¹³ and peak inversions instead of the ray arrivals and ray inver-

sions used in Ref. 23. In this section the peak identification problem is first considered from a statistical point of view, and then Send's least-square method is described; this will allow a better understanding of the approach adopted.

To formulate the identification problem some notions are introduced below. Let an observed (measured) arrival pattern contain J peak arrivals at time instants $\tau_j^{(o)}$, $j=1, \dots, J$. Further, let the background arrival pattern contain I peak arrivals ($I \neq J$, in general) at time instants $\tau_i^{(b)}$, $i=1, \dots, I$. The peak-identification problem consists of determining which of the background arrivals the observed peaks correspond to; it is desirable to associate as many of the observed peaks as possible with background arrivals in order to exploit the maximum available information for the final inversions. Without restriction of generality, it is assumed in the following that the reference and the background sound-speed profiles coincide ($c_0=c_b$), and $\boldsymbol{\vartheta}$ is used instead of $\delta\boldsymbol{\vartheta}$, for notation convenience.

Any monotonically increasing point function $j=\zeta(i)$ from $\{1, 2, \dots, I\}$ into $\{1, 2, \dots, J\}$, realizing a correspondence between background and observed arrivals, is called an *identification function* (cf. Ref. 22). Its domain of definition \mathcal{D}_ζ , not known *a priori*, is in general a subset of $\{1, 2, \dots, I\}$. The cardinality of \mathcal{D}_ζ , i.e., the number of peaks identified through ζ , is denoted by $I' = I'(\zeta)$ ($I' \leq I$, in general). Further, let \mathbf{J} denote the identification space, i.e., the space of all possible identification functions (identifications). In order to avoid unnatural identifications, the identification space is restricted in various ways. A first restriction, introducing some memory effect, is related to the previous identification (in the sequence of tomographic observations); to distinguish between subsequent elements of the observation sequence, the present step (reception) is denoted by K , whereas the previous ones, for which the identification has already been performed, by $K-\lambda$, $\lambda=1, 2, \dots$. The subspace $\mathbf{J}_e(K)$ of $\mathbf{J}(K)$ is introduced as follows:

$$\tilde{\mathbf{J}}_e(K) = \{\zeta \in \mathbf{J}(K) : |\tau_{\zeta(i)}^{(o)}(K) - \hat{\tau}_i(K-1)| < \varepsilon, i \in \mathcal{D}_\zeta\}, \quad (21)$$

where $\hat{\tau}_i(K-1)$ denote the predicted travel times corresponding to the previous identification, $\hat{\tau}_i(K-1) = \sum_j B_{ij} \hat{\vartheta}_j(K-1) + \tau_i^{(b)}$, and $\tau_{\zeta(i)}^{(o)}(K)$ denote the associated observed travel times in the present step K , according to the trial identification ζ . The parameter ε denotes the search radius for determining possible identifications in the present step K . In other words, time windows of size 2ε are set around the predicted arrival times of the previous ($K-1$) step and all observed peaks in the K th reception that fall within each window are considered as possible identifications of the corresponding background arrival.

To exclude elements of $\tilde{\mathbf{J}}_e(K)$ which identify less peaks than the maximum possible, i.e., $I' < \max_{\zeta \in \tilde{\mathbf{J}}_e(K)} (I')$, the space $\tilde{\mathbf{J}}_e(K)$ is further restricted,

$$\mathbf{J}_e(K) = \{\zeta \in \tilde{\mathbf{J}}_e(K) : I'(\zeta) = \max_{\zeta \in \tilde{\mathbf{J}}_e(K)} (I')\}. \quad (22)$$

Two approaches for selecting the best identification among the elements of $\mathbf{J}_e(K)$ are presented below.

A. Peak identification as a statistical estimation problem

The peak-identification problem is treated here as a statistical estimation problem. The conditional joint probability of the model vector *and* trial identification, given the vector of observables, is used to derive maximum-likelihood estimates of these quantities (model vector and trial identification).

By assuming that the elements of the restricted identification space $\mathbf{J}_e(K)$ are equally probable, the *a posteriori* likelihood function $\mathcal{L}(\boldsymbol{\vartheta}, \zeta | \boldsymbol{\tau}_K^{(o)})$ of the model vector $\boldsymbol{\vartheta}$ and trial identification ζ , given the vector of observables $\boldsymbol{\tau}_K^{(o)} = \{\tau_j^{(o)}(K)\}$, can be derived by using the conditional probability law³⁹

$$\begin{aligned} \mathcal{L}(\boldsymbol{\vartheta}, \zeta | \boldsymbol{\tau}_K^{(o)}) &= \Pr[\zeta | \boldsymbol{\tau}_K^{(o)}] \cdot f(\boldsymbol{\vartheta} | \boldsymbol{\tau}_K^{(o)}, \zeta) \\ &= \text{const } f_{X|Y}(\boldsymbol{\vartheta} | \{\tau_{\zeta(i)}^{(o)}(K)\}), \end{aligned} \quad (23)$$

where \Pr and f denote probability and probability density function, respectively. Under the Gaussian hypothesis for the model and noise vector, cf. Eq. (15), and assuming that the covariance matrices \mathbf{R}_{xx} and \mathbf{R}_{nn} are diagonal, the *a posteriori* likelihood function finally takes the form

$$\begin{aligned} \mathcal{L}(\boldsymbol{\vartheta}, \zeta | \boldsymbol{\tau}_K^{(o)}) &= C_3 \exp \left\{ -\frac{1}{2} \sum_{i \in \mathcal{D}_\zeta} \frac{[\{\mathbf{B}\boldsymbol{\vartheta}\}_i + \tau_i^{(b)} - \tau_{\zeta(i)}^{(o)}(K)]^2}{\text{diag}[\mathbf{R}_{nn}]_i} \right. \\ &\quad \left. - \frac{1}{2} \sum_{l=1}^L \frac{[\vartheta_l]^2}{\text{diag}[\mathbf{R}_{xx}]_l} \right\}, \end{aligned} \quad (24)$$

where C_3 is a constant, independent of $\boldsymbol{\vartheta}$ and ζ . By maximizing the likelihood function (24), with respect to $\boldsymbol{\vartheta}$ and ζ , or minimizing the objective function

$$\begin{aligned} S_1(\boldsymbol{\vartheta}, \zeta) &= \sum_{i \in \mathcal{D}_\zeta} \frac{[\{\mathbf{B}\boldsymbol{\vartheta}\}_i + \tau_i^{(b)} - \tau_{\zeta(i)}^{(o)}(K)]^2}{\text{diag}[\mathbf{R}_{nn}]_i} \\ &\quad + \sum_{l=1}^L \frac{[\vartheta_l]^2}{\text{diag}[\mathbf{R}_{xx}]_l}, \end{aligned} \quad (25)$$

maximum-likelihood estimates $\hat{\boldsymbol{\vartheta}}_K$ and $\hat{\zeta}_K$ can be obtained for the model vector and the identification function, respectively, i.e.,

$$S_1(\hat{\boldsymbol{\vartheta}}_K, \hat{\zeta}_K) = \min_{\boldsymbol{\vartheta}, \zeta \in \mathbf{J}_e(K)} S_1(\boldsymbol{\vartheta}, \zeta). \quad (26)$$

Thus, under the assumption of equiprobable trial identifications $\zeta \in \mathbf{J}_e(K)$, the objective function used in the previous section for the maximum-likelihood estimation of the model vector, cf. Eq. (20), can be used in generalized form for determining the maximum-likelihood identification function as well. The minimization of S_1 with respect to $\boldsymbol{\vartheta}$, for given ζ , is performed analytically (see Sec. II A), while the minimization with respect to ζ can be performed only numerically. Thus, for each trial identification, the maximum-likelihood estimate $\hat{\boldsymbol{\vartheta}}(\zeta)$ is calculated from (17). Then the function $S_1(\hat{\boldsymbol{\vartheta}}(\zeta), \zeta)$ is minimized over all trial identifications $\zeta \in \mathbf{J}_e(K)$ by direct numerical comparison. The result-

ing minima ζ_K and $\hat{\boldsymbol{\theta}}_K = \hat{\boldsymbol{\theta}}(\zeta_K)$ are the maximum-likelihood estimates for the identification function and the model vector, respectively.

If a sequence of successive tomographic observations is available, with sufficiently high sampling (observation) rate, it is desirable to make use of the smooth evolution of the system as well. This can be introduced in terms of additional *a priori* information for the model vector; e.g., instead of assuming a zero-mean model vector with covariance matrix \mathbf{R}_{xx} , the model-vector expectation can be constrained to

$$\hat{\boldsymbol{\theta}}_K^{\text{prior}} = g(\hat{\boldsymbol{\theta}}_{K-1}, \hat{\boldsymbol{\theta}}_{K-2}, \dots) = \frac{1}{\Lambda} \sum_{\lambda=1}^{\Lambda} \hat{\boldsymbol{\theta}}_{K-\lambda}, \quad (27)$$

which is the mean of the previous-step estimates $\hat{\boldsymbol{\theta}}_{K-\lambda}$ taken over some prior time interval (memory length Λ). By assuming Gaussian distribution of the model vector around $\hat{\boldsymbol{\theta}}_K^{\text{prior}}$ with relative covariance matrix $\tilde{\mathbf{R}}_{xx}$, which is now a function of $\hat{\boldsymbol{\theta}}_K^{\text{prior}}$, in general, the resulting objective function to be minimized becomes

$$S_2(\boldsymbol{\theta}, \zeta) = \sum_{i \in \mathcal{I}_\zeta} \frac{[\{\mathbf{B}\boldsymbol{\theta}\}_i + \tau_i^{(b)} - \tau_{\zeta(i)}^{(o)}(K)]^2}{\text{diag}[\mathbf{R}_{nn}]_i} + \sum_{l=1}^L \frac{[\boldsymbol{\theta}_l - \hat{\boldsymbol{\theta}}_l^{\text{prior}}(K)]^2}{\text{diag}[\tilde{\mathbf{R}}_{xx}]_l}, \quad (28)$$

where the notation convention $\hat{\boldsymbol{\theta}}_K^{\text{prior}} = \{\hat{\boldsymbol{\theta}}_l^{\text{prior}}(K)\}$ is used. The objective function (28) allows close tracing of the system evolution at the cost of additional *a priori* information $\hat{\boldsymbol{\theta}}_K^{\text{prior}}$ and $\tilde{\mathbf{R}}_{xx}(\hat{\boldsymbol{\theta}}_K^{\text{prior}})$. If the correlation structure of the time series $\{\hat{\boldsymbol{\theta}}_K\}$, $K=1, 2, \dots$, is known, maximum-likelihood estimates of $\hat{\boldsymbol{\theta}}_K^{\text{prior}}$ and $\tilde{\mathbf{R}}_{xx}$ can be obtained at each step K from the past history of the model vector, e.g., by appropriate ARMA modeling.⁴⁰ On the other hand, uncertainties associated with $\tilde{\mathbf{R}}_{xx}$ may cause significant biases, especially in the model-vector estimate which is most susceptible to the form of the probability density function $f_X(\boldsymbol{\theta})$, cf. second term in (28).

In the light of the above remarks, a mixed approach can be introduced, by minimizing the objective function $S_2(\hat{\boldsymbol{\theta}}(\zeta), \zeta)$ as a function of ζ only, with the model-vector taken from (17) for each trial identification. In this way the smooth-evolution constraint is taken into account only for the peak-identification problem, whereas the peak-inversion problem is treated on a more robust zero-mean basis. Although the resulting estimates in this case no longer minimize the objective function S_2 , in this sense being suboptimum with respect to S_2 , such a mixed approach would allow the peak-identification process to take advantage of the prior history, without the inversion process being affected by uncertainties associated with the relative covariance matrix $\tilde{\mathbf{R}}_{xx}$. An objective function of this kind (mixed type) has recently been introduced by the third author in connection with the peak identification problem, independently of statistical considerations. This approach is described below.

B. Peak identification as a least-square problem

The maximum-likelihood objective functions (25) and (28), derived in the previous subsection under the Gaussian assumption, are of least-square type, and they can be introduced by least-square reasoning as well. Such an approach to the identification problem, recently proposed by Send,²³ is based on defining the best identification as the one minimizing the data misfit and the solution deviations from $\hat{\boldsymbol{\theta}}_K^{\text{prior}}$, in the least-square sense. In this connection, a *cost* function is introduced for controlling the corresponding residuals, as follows:

$$S_3(\zeta) = \frac{1}{I'} \sum_{i \in \mathcal{I}_\zeta} \frac{[\{\mathbf{B}\hat{\boldsymbol{\theta}}(\zeta)\}_i + \tau_i^{(b)} - \tau_{\zeta(i)}^{(o)}(K)]^2}{\text{diag}[\mathbf{R}_{nn}]_i} + \frac{\alpha^2 L'}{L'} \sum_{l=1}^{L'} [\hat{\boldsymbol{\theta}}_l(\zeta) - \hat{\boldsymbol{\theta}}_l^{\text{prior}}(K)]^2. \quad (29)$$

The first sum in (29) corresponds to the mean-squared data residuals normalized by the corresponding variances (I' is the number of peaks identified in ζ). The second sum represents a penalty for nonsmooth time evolution; usually only a subset of L' low-order sound-speed modes (the more stable ones) is used for this smoothness condition. The relative weight of the two sums is governed by the parameter α . The significance of the smooth-evolution term for the identification procedure depends on the expected rate of evolution of the underlying ocean system and also on the sampling rate of the specific tomographic experiment. The objective function $S_3(\zeta)$ is used for solving the peak-identification problem, that is, for estimating ζ only. The model vector $\boldsymbol{\theta}$ is estimated from (17), i.e., on a zero-mean basis, for each trial identification ζ .

The function $S_3(\zeta)$ can be interpreted as a special case of $S_2(\hat{\boldsymbol{\theta}}(\zeta), \zeta)$; since, by definition, the number I' of peaks identified is the same for all elements of $\mathbf{J}_e(K)$ (i.e., $I' = \text{const}$), taking $\text{diag}[\tilde{\mathbf{R}}_{xx}]_l = L' / (\alpha^2 I')$, for $l=1, \dots, L'$ and $\text{diag}[\tilde{\mathbf{R}}_{xx}]_l = \infty$, for $l=L'+1, \dots, L$, it can be seen that $S_3(\zeta)$ becomes of the type $S_2(\hat{\boldsymbol{\theta}}(\zeta), \zeta)$. The effect of infinite variances $\tilde{\mathbf{R}}_{xx}$ is that the sound-speed modes of order $l > L'$ are unimportant for the smooth-evolution constraint.

The identification function ζ_K^* which minimizes the objective function (29) is taken as the solution to the peak-identification problem:

$$S_3(\zeta_K^*) = \min_{\zeta \in \mathbf{J}_e(K)} S_3(\zeta). \quad (30)$$

In the light of the previous remarks, the objective function $S_3(\zeta)$ represents a mixed approach to the identification problem. For each trial identification ζ an S_1 -optimum (S_2 -suboptimum) selection is made in (29) for the model vector $\hat{\boldsymbol{\theta}}$. Further, the minimization of (29) over ζ , given $\boldsymbol{\theta} = \hat{\boldsymbol{\theta}}(\zeta)$, leads to an S_2 -optimum (S_1 -suboptimum) solution of the identification problem. The minimization problem (30) is solved in a straightforward way, by direct numerical comparison over *all* possible peak identifications $\zeta \in \mathbf{J}_e(K)$.

The identification ζ_K^* is dependent on a number of tunable parameters: the number L' of sound-speed modes for

the smooth-evolution constraint, the relative weighting (α) of the two terms in the objective function (29), the memory length (Λ) over which the mean of previous mode amplitudes is taken, and also the search radius (ε), i.e., $\zeta_K^* = \zeta_K^*(L', \alpha, \Lambda, \varepsilon)$. Although for an optimum selection tuning is necessary, some guidelines for making first choices for these parameters can be given. Thus the number L' is usually restricted to 1 or 2, depending on how many low-order modes are expected to represent a stable trend. Further, if there is some indication about the rms fluctuation of the modal amplitudes around this trend, a first choice for the parameter α can be made as $\alpha = \sqrt{L'/I}/(\text{rms fluctuation})$; see previous remarks on $S_3(\zeta)$. The memory length Λ should be conformable with the time scale of the particular phenomenon under study and should also ensure the statistical significance of $\hat{\vartheta}_l^{\text{prior}}$; for mesoscale features 1-day memory should be a convenient starting point. Finally, the effect of the search radius ε is nearly binary; beyond a threshold the particular ε value has little effect in the tracking quality—on the other hand, taking ε very large can dramatically increase processing time.

Sometimes, no sensible solutions exist and even the minimized one has a large change in mode amplitudes or a large data residual. For that reason, in addition to the bound on the data residual, also a maximum allowed change in mode amplitude should be set (alternatively, a maximum in the overall objective function). Moreover, special attention must be paid in tracking the main (late) arrival. This arrival is essential because it samples the surface layer of the water column. Since much of the time the main arrival is also the highest one, if the highest peak falls within the search window corresponding to the main arrival, this highest peak is automatically identified as the main arrival. Further, it is allowed for the highest peak to enter the list of possible (trial) identifications for the main arrival even if it lies outside the corresponding search window; in this case, however, it is not automatically identified as the main arrival but it is left to the optimization process to decide.

The above scheme, based on the objective function $S_3(\zeta)$, is used in the following for solving the identification and tracking problem. To initialize the algorithm, a starting value $\hat{\vartheta}_0$ for the model vector is necessary. This is usually obtained from CTD data that are collected during the initial stage of the experiment.

C. Tracking of synthetic data

We return now to the previous synthetic test case in order to assess the performance of the identification and tracking scheme presented in Sec. III B. Relative travel times are used below for performing inversions in the framework of peak-identification process. The reason is that in realistic experiments there is significant uncertainty in absolute peak location, due to the unknown exact position of the transceivers in space and also due to clock drift. Therefore, absolute peak location cannot be used, in general, for first-step inversions.^{1,36} After peak identification and tracking clock drift errors can be removed by averaging over reciprocal travel times of corresponding peaks; further, absolute instru-

ment positions may be adjusted (see Sec. IV below), thus permitting the use of absolute travel times for the final inversions.

The solution- and noise-correlation matrices \mathbf{R}_{xx} and \mathbf{R}_{nn} , respectively, are taken as in Sec. II B. However, since relative-time inversions are considered for peak identification and tracking, the noise-correlation matrix has to be modified accordingly, the error variances in the relative travel times being the sum of the variances corresponding to absolute arrival times (under the assumption that individual error components are uncorrelated). The search radius (ε) for specifying trial identifications is taken 8 ms. To initialize the tracking process the sound-speed profile at the beginning of the experiment (day 0) is assumed known, and the identification for the starting reception is performed in much the same way as in Sec. II B.

For the synthetic case it turned out that, due to the small sampling rate (with respect to the rate of evolution of the episode) of 1 observation per day, tracking should better be performed without the smooth-evolution constraint ($\alpha = 0$). As a matter of fact, because of the large sound-speed change over the 20-day period considered here, there should be several observations per day for the average $\hat{\vartheta}_l^{\text{prior}}$ (over 1–1.5 days) to become statistically significant. In the measured data treated in the next section the sampling rate is high enough and in that case the smoothing term in (29) is used.

Tracking results were found to be identical with the outcome of the manual association performed in Sec. II B based on the complete knowledge of the sound-speed evolution, i.e., the tracks shown in Fig. 9. This conclusion was insensitive to the direction of tracking (forward or backward) and it is a good indication about the robustness of the identification/tracking algorithm. Further results for this case are omitted since they coincide with the results presented in Figs. 10–12.

In order to test the identification/tracking algorithm in a more realistic situation we consider the travel-time data of Fig. 8 distorted by noise. Physical mechanisms introducing noise in the arrival times are, among others, temperature and salinity fluctuations in the water column due to internal waves,^{6,41,42} environmental ambient noise,^{25,5,6} and boundary roughness at the surface of the water column.^{20,43} Even though for the particular environment of THETIS-I experiment, with sound-speed profiles close to linear, the estimated cumulative distortion levels in arrival times for the T3–T6 transceiver pair lie below 1 ms,^{6,36,42,43} significantly higher noise levels, of 2 and 4 ms (rms value), respectively, are considered below. The purpose of artificially exaggerating the distortion of peak locations in the synthetic case is to test the sensitivity of the identification/tracking algorithm and the inversion scheme.

Figure 13 shows the distorted peak locations using uniformly distributed noise of zero mean and rms value 2 ms. Tracking is performed in both forward and backward directions, and the averaged results from the identification and tracking procedure are also marked in Fig. 13, identified peaks being within circles and resulting tracks being shown through solid lines. For performing inversions the correlation matrix \mathbf{R}_{nn} has been modified to take account of the addi-

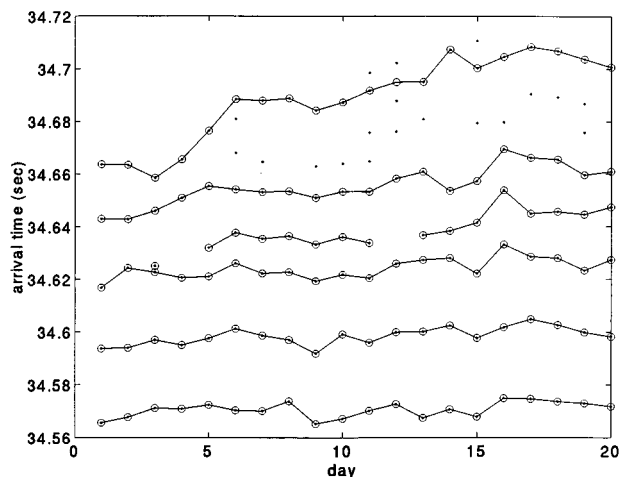


FIG. 13. Automatically obtained, forward/backward-averaged tracks from identification/tracking algorithm. Actual peak locations, marked by dots (\cdot), have been distorted by uniformly distributed noise of zero mean and 2-ms rms value.

tional noise. Further, a larger search window (of 10-ms radius) has been applied. The influence of the tracking direction can be seen on day 12 in the case of the arrival 6 which is associated with either of the last two observed peaks, depending on the direction of tracking; the corresponding averaged track passes through neither of these peaks but through their middle. By comparing Figs. 9 and 13 it is seen that in all other cases the identification/tracking scheme manages to find the correct tracks, independently of tracking direction.

Further worsening of the synthetic data is shown in Fig. 14, in which noise of 4-ms rms value is added to the initial arrival times of Fig. 8. The tracking results are still very satisfactory in regard to the identification of the correct peaks, with an exception of peak 5 on day 16, which is misidentified by a small amount. Further, it is remarkable that the identification/tracking results were found to be in-

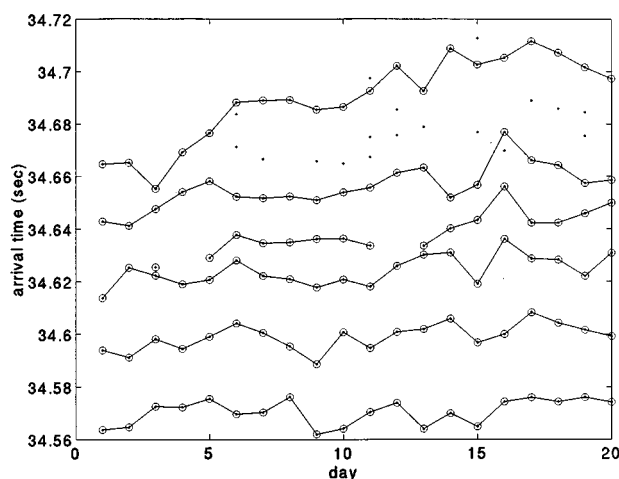


FIG. 14. Automatically obtained, forward/backward-averaged tracks from identification/tracking algorithm. Actual peak locations, marked by dots (\cdot), have been distorted by uniformly distributed noise of zero mean and 4-ms rms value.

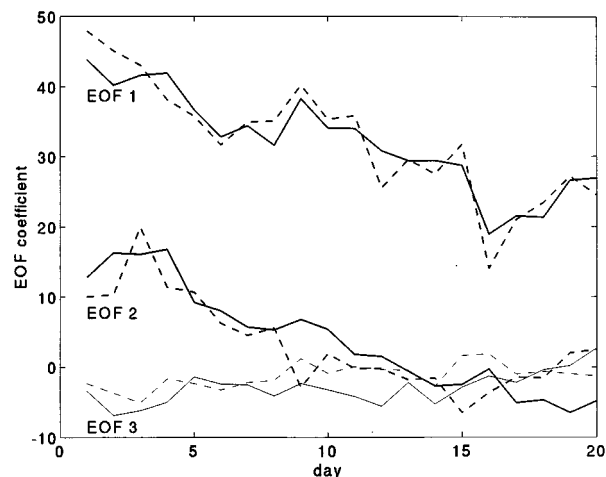


FIG. 15. Comparison of inversion results for the first three EOF coefficients (dashed lines) to the input data (solid lines); inversions based on the automatically obtained peak tracks of Fig. 14 (noisy data).

sensitive to the tracking direction. Figure 15 shows a comparison of the inversion results for the first three EOF coefficients (dashed lines), corresponding to the tracks of Fig. 14 (4-ms noise), with the initial coefficients (solid lines). Further, Fig. 16 shows the sequence of the corresponding retrieved sound-speed anomaly profiles (dashed lines), with respect to the linear profile, as compared to the initial profiles (solid lines). Finally, in Fig. 17 the evolution of depth-averaged sound-speed anomalies are shown for the three layers: 0–100, 100–600, and 0–1000 m. It is seen from these figures that, even in the presence of excessive noise in the arrival times, the identification/tracking algorithm works properly, and the main features of the sound-speed evolution within the water column can be still retrieved satisfactorily.

IV. APPLICATION TO THETIS-I DATA

In this section the peak inversion scheme is applied to the measured data corresponding to the T3–T6 transceiver

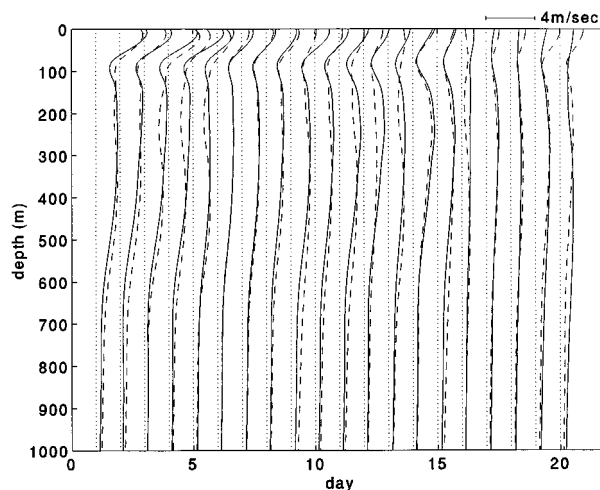


FIG. 16. Comparison between the retrieved sound-speed anomaly profiles, with respect to the linear profile (dashed lines), and the corresponding synthetic anomaly profiles (solid lines), cf. Fig. 7; inversions based on the automatically obtained peak tracks of Fig. 14 (noisy data).

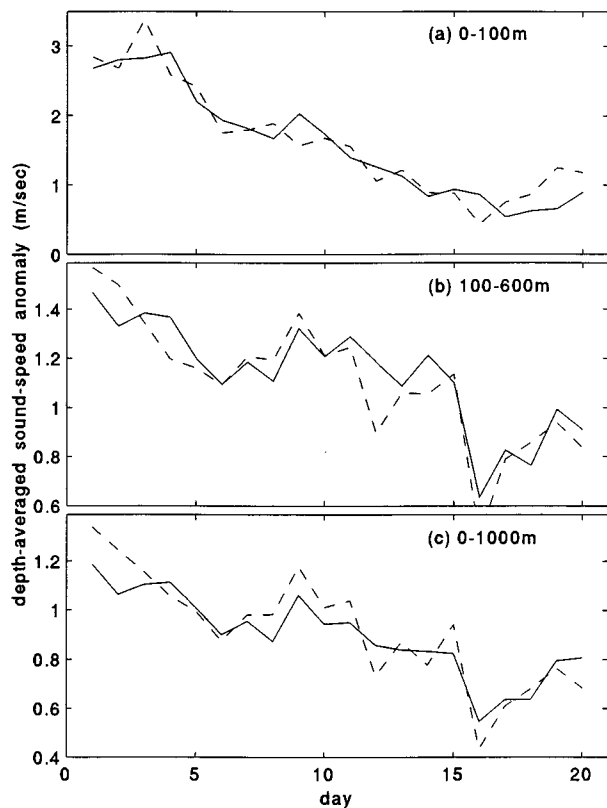


FIG. 17. Comparison of inversion results for the depth-averaged sound-speed anomalies (dashed lines) to the corresponding input anomalies (solid lines); inversions based on the automatically obtained peak tracks of Fig. 14 (noisy data). (a) Layer 0–100 m, (b) layer 100–600 m, (c) layer 0–1000 m.

pair from the THETIS-I tomographic experiment conducted during Winter 1991–1992 (12/14/1991–4/10/1992) in the Gulf of Lions/western Mediterranean Sea; see Fig. 1. The main objective of this experiment was to monitor deep convection phenomena occurring in this area due to prevailing Mistral winds.^{24,44–46} A typical feature of the region, prior to the onset of convection, is the presence of a warm and salty subsurface layer between 100- and 600-m depth, representing the Levantine intermediate water (LIW) originating from the eastern Mediterranean basin.^{44,46} Vertical mixing induced by deep convection causes homogenization and significantly weakens the temperature and salinity stratification. Consequently convection has a signature in the sound-speed distribution in the water column, and this forms the basis for using acoustic tomography to monitor the phenomenon.

The tomographic array is shown in Fig. 1. It consists of six tomographic transceivers (denoted by T1–T6) located at a nominal depth of 150 m, emitting and receiving broadband tomographic signals of bandwidth 100 Hz and central frequency 400 Hz. Further features of the instrument and signal design are omitted here; a detailed description of the experimental setting and performance can be found elsewhere.^{36,45} Due to instrument malfunction the temporal coverage by tomographic data was quite irregular. The longest time series of good-quality reciprocal receptions covers 60 days (mid-December 1991 to mid-February 1992) and corresponds to the T3–T6 instrument pair. In the following we concentrate

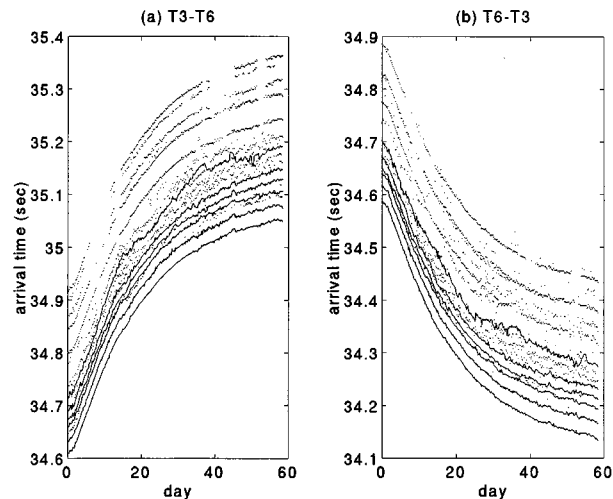


FIG. 18. THETIS-I experiment: observed peak locations, marked by dots (\cdot), from the T3–T6 transceiver pair, and automatically obtained peak tracks, marked by solid lines. (a) T3 receiving/T6 emitting, (b) T6 receiving/T3 emitting.

on this pair, which formed the basis for the synthetic case as well. Further, since both instruments emit and receive signals (reciprocal transmissions) we use below the notation T3–T6 to denote T3 receiving and T6 emitting, and T6–T3 to denote T6 receiving and T3 emitting. The T3–T6 time series has a sampling rate of 30 receptions per day, whereas the rate for T6–T3 time series is 20 receptions per day. To have a common basis for both time series and also to increase reliability, 0.2-day averages are formed by grouping every six T3 receptions and every four T6 receptions, and taking averages, respectively.

In Fig. 18 the peak locations (dots) along with the automatically obtained tracks (solid lines) for the two reciprocal receptions (T3–T6 and T6–T3) are shown, after mooring-motion (navigation) correction; the starting day of the experiment is denoted as day 0. The systematic trend of peaks and tracks observed in this figure is due to differential clock drift between instruments T3 and T6, which over the period of 60 days is too large to allow for absolute-time inversions. Six tracks, corresponding to the six arrivals of the background pattern (cf. Fig. 4) were obtained using the identification/tracking scheme described in Sec. III B. Additional peaks observed in Fig. 18 after the late (uppermost) track correspond to bottom-reflected arrivals, not exploited here since they are affected by the geoacoustic characteristics of the bottom.¹³

Due to the small number of peaks tracked, the identification/tracking procedure was found occasionally to be quite sensitive when two or more arrivals could not be identified in a reception. The reason is that in such cases the inversion is based on a very small number of remaining peaks, thus resulting in a poor prediction of arrival times used for specifying possible (trial) identifications in the next reception. To avoid such malfunctions, whenever two or more arrivals could not be identified in a reception, their time locations, used for the inversions, were assumed to remain unchanged from those of the previous reception. The

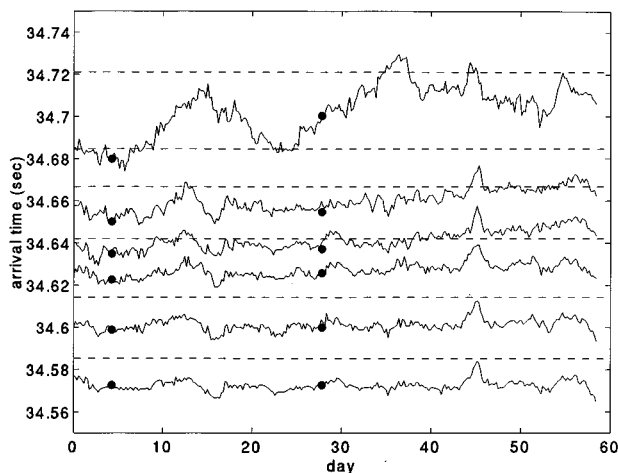


FIG. 19. THETIS-I experiment: Mutually averaged and offset calibrated peak tracks corresponding to the T3–T6 pair. Background arrival times are marked by dashed lines. Arrival-time predictions corresponding to CTD data (calculated from the first-order perturbation formula) are marked by filled circles (●).

memory length in the identification/tracking procedure, over which the previous mode amplitudes were averaged, was taken equal to 1 day ($\Lambda=5$), whereas the first two EOFs were used for the smoothness condition, i.e., $L'=2$ in Eq. (29), since higher-order modes are expected to represent small details rather than systematic changes in the sound-speed structure.⁴⁵ Further, the weighting coefficient α used was typically in the range $\alpha=0.25-0.5$, and the search radius ranged from 5 ms for the early arrivals to 10 ms for the late ones.

The solution-correlation matrix \mathbf{R}_{xx} , needed for the inversions, was taken to be diagonal, and its elements were estimated from principal component analysis of historical hydrographic bottle data covering the area of interest. More specifically, the rms values of the EOF coefficients were found: $\vartheta_{1,\text{rms}}=35.8$, $\vartheta_{2,\text{rms}}=18.1$, $\vartheta_{3,\text{rms}}=6.9$, $\vartheta_{4,\text{rms}}=7$, $\vartheta_{5,\text{rms}}=5$. Further, the noise-correlation matrix \mathbf{R}_{nn} is taken as in Sec. II B.

After having obtained the tracks associated with each of the six background arrivals in the two reciprocal receptions, the clock drift can be eliminated by averaging arrival times of corresponding tracks. The resulting tracks should be the input data for the final tomographic inversions. However, there still remains an uncertainty in these data in regard to the exact origin of the τ_i axis, associated with the exact location of the anchor of each mooring during deployment. Consequently, the exact distance R between moorings T3 and T6 remains unknown, resulting in an extra unknown offset of the peak locations. In order to determine this offset we exploit CTD data collected during the experiment at the transceiver locations. In particular, two sets of CTD data are available for the section T3–T6, centered on days 4.3 and 27.8, respectively.

The offset-calibration results are shown in Fig. 19. The background arrival times are shown in this figure through dashed horizontal lines, whereas the theoretically predicted arrival times [using the first-order perturbation formula (7)]

corresponding to CTD data are marked by filled circles (●). Finally, the six tracks, obtained by averaging over corresponding reciprocal tracks in Fig. 18, and offset by -19 ms (i.e., shifted altogether by 19 ms in the negative t direction) to adjust for the horizontal distance between instruments, are shown by solid lines in Fig. 19. It is seen that, after clock drift correction and offset calibration, the experimental arrivals match quite well with the predicted arrival times corresponding to the CTD data; note that a CTD measurement is a point measurement while, on the other hand, tomography gives a range-averaged view of the water properties.

On the basis of travel-time anomalies shown in Fig. 19 (with respect to the background arrival times), absolute-time tomographic inversions are performed. The inversion results are shown in Fig. 20 as a color plot of the sound-speed anomalies, with respect to the linear background profile. It is seen from this figure that sound-speed perturbations both in the surface layer and in the LIW subsurface layer decrease toward the end of the 60-day period, indicating gradual cooling and homogenization of the water column (mixed-layer conditions establish). In the surface layer the variability is larger than in deeper layers, which is also reasonable. In the beginning of the experiment maximum sound-speed anomalies close to 4 m/s are calculated at the surface with a strong tendency to decrease; in two weeks' time the sound-speed anomaly at the surface reduces to -1 m/s, corresponding to a temperature decrease of about 1.5°C . This first cooling period is followed by a 1-week-long rewarming period (increase of sound speed at the surface) and then by a second period of cooling which lasts up to the end of the 60-day period. In regard to the LIW subsurface layer, there seems to be no significant cooling trend during the first 40 days. However, after day 40 (23 January) the sound speed in the LIW layer starts gradually decreasing as well; this is an indication for vertical mixing in the water column.

In Fig. 21 time series of depth-averaged sound-speed anomalies (with respect to the linear profile) over the layers 0–100 (surface layer), 100–600 (LIW layer), and 0–1000 m are shown. The inversion results are denoted by heavy solid lines, while the rms error estimates⁴⁷ are indicated by light lines about the inversion time series. Depth averages calculated from the CTD data are marked by filled circles (●). It is seen that the overall agreement of the tomography time series with the CTD data is satisfactory; the largest misfit, about 0.2 m/s, occurs in the 100- to 600-m layer on day 27.8. Similar remarks can be made for the temperature evolution as previously.

In Fig. 22 the retrieved sound-speed anomaly profiles (with respect to the linear profile), marked through dashed lines, are compared with the corresponding CTD profiles (solid lines). One-day averages of the inversion results were considered, in order to take account of the temporal spreading of the CTD data. The retrieved anomaly profiles compare satisfactorily with the corresponding CTD profiles in both cases; maximum differences come up to 0.25 m/s locally. The more systematic deviations occurring on day 27.8 within the LIW layer can be explained in terms of the travel times shown in Fig. 19, where the peak tracks of arrivals 4 and 5,

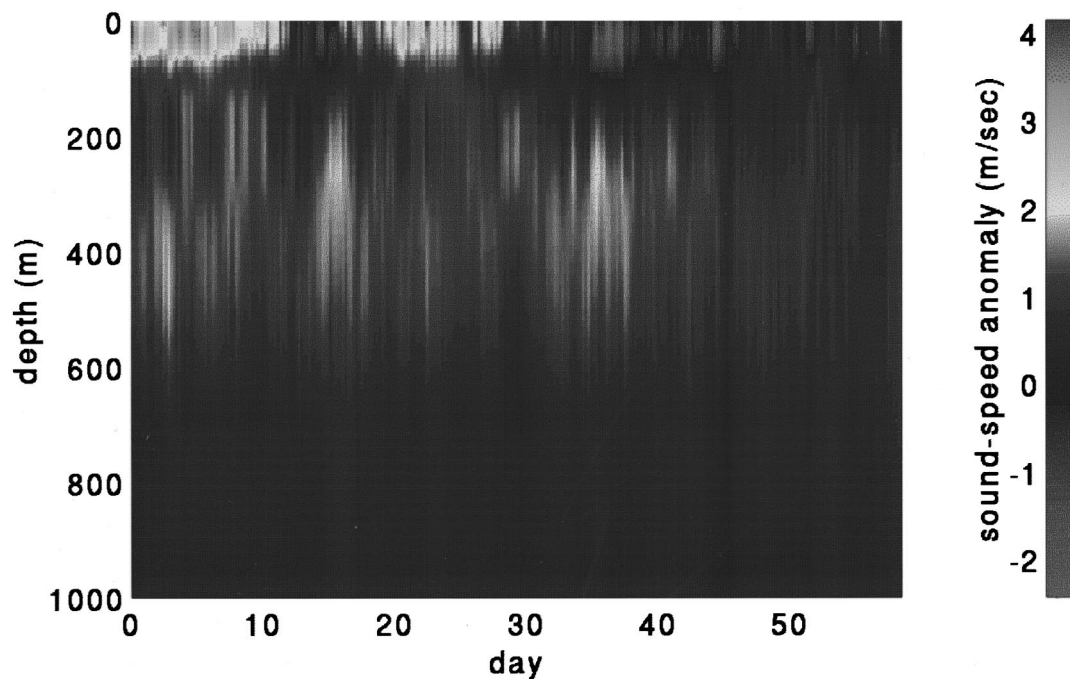


FIG. 20. THETIS-I experiment/inversion results: Evolution of the retrieved sound-speed anomaly, with respect to the linear profile, over the period of 60 days; inversions based on the automatically obtained peak tracks of Fig. 19.

sampling the LIW layer,¹³ are slightly delayed, by approximately 3 ms, with respect to the predicted arrival times. Such a time delay considered over the range of 52 km may cause deviations of the above magnitude in the sound speed, and this also gives an idea of the sensitivity of the tomographic system.

V. DISCUSSION AND CONCLUSIONS

In a recent work¹³ the notion of peak arrivals had been introduced as a vehicle to model arrival-time perturbations, due to variations of the sound speed within the water column. In the present work the inverse problem of performing ocean tomography based on peak arrivals is addressed.

The common observables in an experimental arrival pattern are the more significant peaks (local maxima), not necessarily corresponding to the arrival of single modes (modal arrivals) or along distinct eigenrays (ray arrivals). Peak arrivals, defined as the local maxima of the arrival pattern, constitute direct theoretical counterparts of experimentally observed peaks, and hence offer a complete modeling of experimental observables, even in cases that ray or modal arrivals cannot be resolved. Moreover, the peak-arrival approach is free of any restrictive conditions or hypotheses concerning the signal or the environment or the wave-propagation model.

Using the definition of peak arrivals, the influence matrix relating sound-speed variations with induced travel-time perturbations can be expressed in closed form by means of appropriate Fréchet derivatives of the point functionals τ_i with respect to the sound-speed field. Consequently the calculation of the influence matrix is performed in a *single* di-

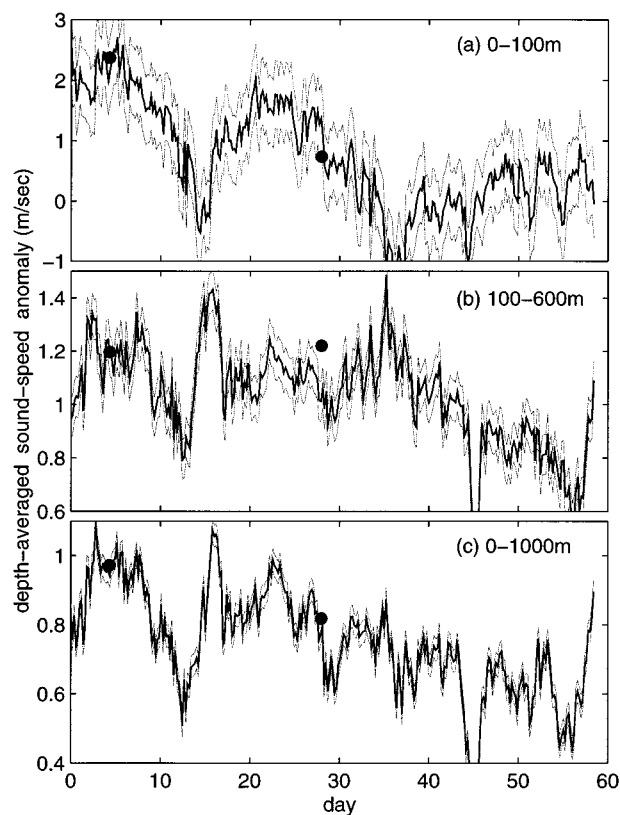


FIG. 21. THETIS-I experiment/inversion results: Evolution of depth-averaged sound-speed anomalies (heavy solid lines), with respect to the linear profile; light lines indicate rms error estimates. CTD data are marked by filled circles (●). (a) Layer 0–100 m, (b) layer 100–600 m, (c) layer 0–1000 m.

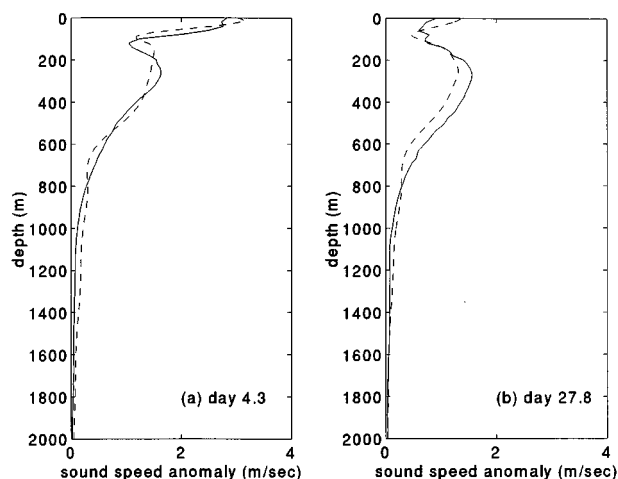


FIG. 22. THETIS-I experiment/inversion results: Comparison between retrieved sound-speed anomaly profiles (dashed lines) and corresponding CTD anomaly profiles (solid lines): (a) day 4.3, (b) day 27.8.

rect run, rather than using a series of runs for different perturbed sound-speed profiles and forming finite differences over corresponding travel times.

The ability of the peak-inversion scheme to retrieve the sound speed has been demonstrated by first considering a synthetic case. The association between background arrivals and observed peaks was initially obtained from a direct perturbation study based on the knowledge of the sound-speed profiles. This knowledge, though available in a synthetic case, is not available in a real tomographic experiment, where the sound speed is a basic quantity sought. In that case the peak-identification and tracking problem arises. Traditionally peak tracking is considered separately from the peak-identification problem. A novel approach which attempts to unify these steps and further relate them to the inversion procedure was recently developed in the context of ray tomography.²³ The basic idea is to test *all* possibilities of associating observed peaks with predicted ones via trial inversions, and finally select the best identification with respect to a least-square criterion. This approach was further developed and extended here toward two directions. On the one hand, it is given a probability-theoretic foundation, as a joint maximum-likelihood estimation problem. On the other hand, it is extended to treat peak arrivals, defined in Ref. 13.

The feasibility of peak tomography (identification, tracking, inversion) has been demonstrated using both synthetic and measured data. In the synthetic case the scheme was tested with noise-free as well as with noisy data, and its performance was satisfactory in both cases; it turned out that in most cases the identification/tracking algorithm could track the correct peaks, independently of tracking direction, and further that the retrieved sound-speed profiles were in good agreement with the input data, with larger deviations in the noisy case, as expected. Measured data from the THETIS-I experiment were also used for performing peak-identification, tracking, and tomographic inversions. The peak-identification and tracking algorithm proved successful with the measured data as well, even though it sometimes involved hundreds of trial inversions. Final inversion results

were found to be in good agreement with CTD observations conducted in the area of the experiment.

A limitation of the peak-tomography scheme presented is the fact that the maximum number of arrivals that can be identified and subsequently used for tomographic inversions is limited to the number of background peak arrivals. In case there are more peaks in a reception than background arrivals (such occasions appeared here both with the synthetic and the measured data), the information contained in the additional peaks' locations cannot be exploited, unless an iterative scheme is developed. A further limitation of the scheme might be the amount of CPU time needed for performing forward calculations, depending on the model used for the direct problem; up to now normal-mode theory has been considered for modeling range-independent environments. A possible way to solve this problem would be to use a hybrid approach: ray theory for the early arrivals and mode theory for the late ones, in connection with the peak-arrival approach.

ACKNOWLEDGMENTS

The authors would like to thank Michael Taroudakis, John Papadakis, Yves Desaubies, Fabienne Gaillard, and Didier Mauuary for fruitful interaction on ocean tomography issues, and also the reviewers for helpful comments. The present work was supported by the European Union under MAST Project No. 0008-C/THETIS-I.

- ¹W. H. Munk and C. Wunsch, "Ocean acoustic tomography: A scheme for large scale monitoring," *Deep-Sea Res.* **26A**, 123–161 (1979).
- ²The Ocean Tomography Group, "A demonstration of ocean acoustic tomography," *Nature* **299**, 121–125 (1982).
- ³J.L. Spiesberger and P.F. Worcester, "Perturbations in travel time and ray geometry due to mesoscale disturbances: A comparison of exact and approximate calculations," *J. Acoust. Soc. Am.* **74**, 219–225 (1983).
- ⁴B.M. Howe, P.F. Worcester, and R.C. Spindel, "Ocean acoustic tomography: Mesoscale velocity," *J. Geophys. Res.* **92**, 3785–3805 (1987).
- ⁵Y. Desaubies, "Ocean acoustic tomography," in *Oceanographic and Geophysical Tomography*, edited by Y. Desaubies, A. Tarantola, and J. Zinn-Justin (Elsevier, Amsterdam, 1990), pp. 159–202.
- ⁶W.H. Munk, P.F. Worcester, and C. Wunsch, *Ocean Acoustic Tomography* (Cambridge U.P., New York, 1995).
- ⁷W.H. Munk and C. Wunsch, "Ocean acoustic tomography: Rays and modes," *Rev. Geophys. Space Phys.* **21**, 777–793 (1983).
- ⁸L. Brekhovskikh and Y. Lysanov, *Fundamentals of Ocean Acoustics* (Springer-Verlag, New York, 1982).
- ⁹E.C. Shang, "Ocean acoustic tomography based on adiabatic mode theory," *J. Acoust. Soc. Am.* **85**, 1531–1537 (1989).
- ¹⁰P.J. Sutton, W.M.L. Morawitz, B.D. Cornuelle, G. Masters, and P.F. Worcester, "Incorporation of acoustic normal mode data into tomographic inversions in the Greenland sea," *J. Geophys. Res.* **99**, 12 487–12 502 (1994).
- ¹¹M.I. Taroudakis and J.S. Papadakis, "Modal inversion schemes for Ocean Acoustic Tomography," *J. Comp. Acoust.* **1**, 395–421 (1993).
- ¹²P.J. Sutton, P.F. Worcester, G. Masters, B.D. Cornuelle, and J.F. Lynch, "Ocean mixed layers and acoustic pulse propagation in the Greenland sea," *J. Acoust. Soc. Am.* **94**, 1517–1526 (1993).
- ¹³G.A. Athanassoulis and E.K. Skarsoulis, "Arrival-time perturbations of broadband tomographic signals due to sound-speed disturbances. A wave-theoretic approach," *J. Acoust. Soc. Am.* **97**, 3575–3588 (1995).
- ¹⁴G.A. Athanassoulis, J.P. Papadakis, E.K. Skarsoulis, and M.I. Taroudakis, "A comparative study of two wave-theoretic inversion schemes in ocean acoustic tomography," in *Full Field Inversion Methods in Ocean and Seismo-acoustics*, edited by O. Diachok, A. Caili, P. Gerstoft, and H. Schmidt (Kluwer, Dordrecht, 1995), pp. 127–132.
- ¹⁵J.L. Spiesberger, R.C. Spindel, and K. Metzger, "Stability and identifica-

- tion of ocean acoustic multipaths," J. Acoust. Soc. Am. **67**, 2011–2017 (1980).
- ¹⁶G.R. Legters, N.L. Weinberg, and J.G. Clark, "Long-range Atlantic acoustic multipath identification," J. Acoust. Soc. Am. **73**, 1571–1580 (1983).
- ¹⁷J.L. Spiesberger and K. Metzger, "Basin-scale tomography: A new tool for studying weather and climate," J. Geophys. Res. **96**, 4869–4889 (1991).
- ¹⁸P.F. Worcester, "An example of ocean acoustic multipath identification at long range using both travel time and arrival angle," J. Acoust. Soc. Am. **70**, 1743–1747 (1981).
- ¹⁹R. Hippenstiel, E. Chaulk, and J.H. Miller, "An adaptive tracker for partially resolved acoustic arrivals with application to ocean acoustic tomography," J. Acoust. Soc. Am. **92**, 1759–1762 (1992).
- ²⁰J.H. Miller, J.F. Lynch, C.S. Chiu, E.L. Westreich, J.S. Westreich, R. Hippenstiel, and E. Chaulk, "Acoustic measurements of surface gravity wave spectra in Monterey Bay using mode travel-time fluctuations," J. Acoust. Soc. Am. **94**, 954–974 (1993).
- ²¹F.R. Martin-Lauzer and D. Mauuary, "Probabilistic ray identification: A new tool for ocean acoustic tomography," in Proceedings of ICASSP 94, Adelaide, 1994.
- ²²D. Mauuary, Ph.D. thesis, Institut National Polytechnique de Grenoble, 1994.
- ²³U. Send, "Peak tracking by simultaneous inversion: Toward a one-step acoustic tomography analysis," J. Atmos. Ocean. Technol. (in press).
- ²⁴The THETIS Group, "Open-ocean deep convection explored in the Mediterranean," EOS, Trans. Am. Geophys. U. **75**, 217, 219–221 (1994).
- ²⁵R.C. Spindel, "Signal processing in ocean tomography," in *Adaptive Methods in Underwater Acoustics*, edited by H. Urban (Reidel, Dordrecht, 1985).
- ²⁶R.C. Spindel, "An underwater acoustic pulse compression system," IEEE Trans. Acoust. Speech Signal Proc. **ASSP-27**, 723–738 (1979).
- ²⁷K. Metzger, Jr., Ph.D. thesis, University of Michigan, Ann Arbor, 1983.
- ²⁸In the geophysical literature sometimes the term observation matrix is used for $\{B_{ij}\}$. The term influence matrix is preferred here since it better describes the role of $\{B_{ij}\}$ in relating $\{\delta\theta_i\}$ with $\{\delta\tau_i\}$.
- ²⁹C.A. Boyles, *Acoustic Waveguides: Applications to Oceanic Science* (Wiley, New York, 1984).
- ³⁰L. Brekhovskikh and O. Godin, *Acoustics of Layered Media II: Point Sources and Bounded Beams* (Springer-Verlag, Berlin, 1992).
- ³¹A. Tarantola, *Inverse Problem Theory* (Elsevier, New York, 1987).
- ³²H.L. van Trees, *Detection, Estimation, and Modulation Theory* (Wiley, New York, 1968), Part I.
- ³³J.N. Franklin, "Well-posed stochastic extensions of ill-posed linear problems," J. Math. Anal. Appl. **31**, 682–716 (1970).
- ³⁴C.R. Rao, *Linear Statistical Inference and its Applications* (Wiley, New York, 1973).
- ³⁵K. Aki and P.G. Richards, *Quantitative Seismology. Theory and Methods* (Freeman, San Francisco, 1980).
- ³⁶"THETIS-I: Enhanced acoustic tomography and its application to circulation and deep convection in the western Mediterranean," edited by F. Schott, Final Report, EC-MAST Project No. 0008–C, 1993.
- ³⁷F.B. Jensen and M.C. Ferla, "SNAP: The SACLANTCEN normal-mode acoustic propagation model," SM-121 SACLANT Undersea Research Center, La Spezia, Italy, 1979.
- ³⁸M.B. Porter and E.L. Reiss, "A numerical method for ocean acoustic normal modes," J. Acoust. Soc. Am. **76**, 244–252 (1984).
- ³⁹A. Papoulis, *Probability, Random Variables, and Stochastic Processes* (McGraw-Hill, Singapore, 1991).
- ⁴⁰A.M. Yaglom, *An Introduction to the Theory of Stationary Random Functions* (Prentice-Hall, Englewood Cliffs, NJ, 1962).
- ⁴¹*Sound Transmission Through a Fluctuating Ocean*, edited by R. Dashen, W.H. Munk, K.M. Watson, and F. Zachariasen (Cambridge U.P., New York, 1979).
- ⁴²S.M. Flatte and R. Stoughton, "Predictions of internal-wave effect on the ocean acoustic coherence, travel-time variance, and intensity moments for very long-range propagation," J. Acoust. Soc. Am. **84**, 1414–1424 (1988).
- ⁴³J.F. Lynch, J.H. Miller, and C.S. Chiu, "Phase and travel-time variability of adiabatic acoustic normal modes due to scattering from a rough sea surface, with applications to propagation in shallow-water and high-latitude regions," J. Acoust. Soc. Am. **85**, 83–89 (1989).
- ⁴⁴F. Schott and K. Leaman, "Observation with acoustic doppler current profilers in the convection regime in the Golfe du Lion," J. Phys. Oceanogr. **21**, 558–574 (1991).
- ⁴⁵U. Send, F. Schott, F. Gaillard, and Y. Desaubies, "Observation of a deep convection regime with acoustic tomography," J. Geophys. Res. **100**, 6927–6941 (1995).
- ⁴⁶M. Rhein, "Deep water formation in the western Mediterranean," J. Geophys. Res. **100**, 6943–6959 (1995).
- ⁴⁷For a particular layer the rms error estimate is given by $(\bar{\phi}\mathbf{D}_{xx}\bar{\phi}')^{1/2}$, where $\bar{\phi}$ is a row vector containing the averages of the sound-speed modes $\{\phi_i\}$, over the layer, and \mathbf{D}_{xx} is the *a posteriori* covariance matrix of the model vector.